
Article:
Liu, Shunpan, Zhao, Xing orcid.org/0000-0003-4000-0446, Wu, Yihao et al. (4 more authors) (2022) Efficiency Improvement of Dual-Receiver WPT Systems Based on Partial Power Processing Control. IEEE Transactions on Power Electronics. pp. 7456-7469. ISSN 0885-8993

https://doi.org/10.1109/TPEL.2021.3138435

IEEE Transactions on Power Electronics

Efficiency Improvement of Dual-Receiver WPT Systems Based on Partial Power Processing Control

Journal:	*IEEE Transactions on Power Electronics*
Manuscript ID	TPEL-Reg-2021-04-1042.R1
Manuscript Type:	Regular Paper
Date Submitted by the Author:	23-Aug-2021
Complete List of Authors:	Liu, Shunpan; Southwest Jiaotong University, School of Electrical Engineering Zhao, Xing; Hong Kong Polytechnic University, Electrical Engineering Wu, Yihao; Southwest Jiaotong University, Zhou, Lingyun; Southwest Jiaotong University, School of Electrical Engineering Li, Yong; Southwest Jiaotong University, School of Electric Engineering Mai, Ruikun; Southwest Jiaotong University, Eletrical Engineering Department He, Zhengyou; SouthWest Jiaotong University, School of Electrical Engineering
Keywords:	DC-AC power conversion, Inductive energy storage, Industrial electronics

Efficiency Improvement of Dual-Receiver WPT Systems Based on Partial Power Processing Control

Shunpan Liu, *Student Member, IEEE*, Xing Zhao, *Member, IEEE,* Yihao Wu, *Student Member, IEEE*, Lingyun Zhou, *Student Member, IEEE*, Yong Li, *Senior Member, IEEE*, Ruikun Mai, *Member, IEEE*, and Zhengyou He, *Senior Member, IEEE*

***Abstract*—In Wireless Power Transfer (WPT) system for light electric vehicles, adopting dual receivers on the receiver side is an available way to offer a high-current power supply. In this paper, the Partial Power Processing (PPP) control method is proposed for optimizing the power loss of the dual-receiver WPT system. With the PPP control method, only one of the active rectifiers will be regulated by the variable angle phase shift (VAPS) modulation to adjust the required power under different load power demands and misalignment situations. As a result, the switching loss of the two active rectifiers, which is the significant power loss on the receiver side, can be dramatically reduced, especially with a high operating frequency. The experimental results show that compared with the conventional power distribution method based on impedance matching with VAPS, the proposed PPP control method can increase the efficiency by 6~7% with misalignment situations, achieving the overall efficiency as high as >92% at the heavy load.**

***Index Terms*—Wireless power transfer (WPT), light electric vehicles (LEVs), dual receivers, power distribution method, partial power processing (PPP).**

I. Introduction

Along with the rapid development of automation industrial production and logistics transportation, Light Electric Vehicles (LEVs) are rapidly spreading worldwide, such as automated guided vehicles, industrial robots, and unmanned vehicles. The traditional fixed-cable-charging system has become an obstacle to improving the automation level of LEVs and further increasing the work efficiency of production and logistics management. Nowadays, Wireless Power Transfer (WPT) technology has become popular and has been widely applied in various applications, e.g., consumer electronics [1]-[4], LEDs [5], [6], and electric vehicles [7]-[12]. Due to its merits, including safety, convenience, and reliability, the WPT system can serve as a flexible and automated power supply solution for LEVs [13]-[19].

While using WPT technology to charge LEVs, several key features need to be considered: 1) To satisfy the voltage class and shorten the charging time, the low-voltage and high-current power supply system is required [14], [18], which is typically 24V/36V/48V and more than 50A; 2) LEVs are so compact that the installation space of which is small, hence the coil size of the WPT system is limited [13], [16]; 3) The heat dispersion of the receiver side in such a compact space is a severe issue with the required high charging current and high operating frequency [14], [17], [18].

For the low-voltage and high-current output WPT system, reducing the power loss caused by the equivalent series resistances (ESRs) of the receiver coil, which always under the high current stress, is the first challenge. To release the current stress in the receiver coil, the dual-receiver topology, including the dual receiver coils and the dual rectifiers, is applied in [20], [21]. Meanwhile, with two paralleled rectifiers, the requirements on the conducting resistance of power MOSFETs can be halved. Additionally, the LCC-LCC compensation network can offer an extra control variable to release the current stress and the ampacity requirement in the receiver coil further, which is also attractive in the high-current output WPT system, [20], [21]. This compensation network can also reduce the harmonic currents and the corresponding power loss, especially in short air gap applications [18], [22].

For the feature of the limited volume, the receiver coil size of the WPT system should be small, which leads to a small mutual inductance and weakens the system power transfer capacity. To solve this issue, increasing the system operating frequency is a general method to enhance the system power density, which is consensual in power electronic transformers [23], [24].

For the heat dispersion issue on the receiver side, the requirement for the power loss of the receiver is stringent. In a WPT system, the power loss on the receiver side can be divided into the ESRs loss of the receiver coils and the elements in compensation networks, the switching loss and the conducting loss of rectifiers. Currently, the efficiency optimization method of the dual-receiver WPT system is in short supply. In a dual-transmitter WPT system, which is a symmetric topology and has two transmitter coils and two inverters, a classical but conventional method based on impedance matching for improving the overall efficiency is proposed [25], [26]. In this method, the equivalent load impedance of each transmitter is regulated to be equal strictly. Thus, the coil loss and the conducting loss can be minimized, and optimal efficiency is achieved even under misalignment conditions. Similar ideas and methods have been widely recognized in some WPT systems with multi-receivers or multi-loads [27], [28] and can also be utilized in the dual-receiver WPT system.

However, the vast switching loss on the rectifiers still lacks sufficient research attention in these methods above. In the low-voltage and high-current output WPT systems, the active rectifier and MOSFETs with ultra-low conducting resistance are always expected for reducing the rectifier conducting loss. However, this kind of MOSFETs, generally are the low-voltage Si MOSFETs, always suffers from the slow switching speed and leads to significant switching loss in the rectifier, especially with a high operating frequency. Though the ESRs loss of the receiver coil can be well-limited by adopting the dual-receiver topology and designing the LCC-LCC compensation network, the switching loss of the rectifier cannot be easily optimized by designing the circuit topology. Thus, the switching loss even occupies a significant proportion of the overall power loss.

In general, the optimization of switching loss is still an urgent problem for the compact WPT system. With the rapid

development of power electronic materials, some novel SiC [29], [30] and GaN [31]-[33] switching devices are adopted in the WPT systems for improving the switching performance. However, replacing all the switching elements with these novel switching devices will increase the system cost dramatically. Some modulation and control methods are proposed for achieving Zero Voltage Switching (ZVS) operations. In [34], an auxiliary variable inductor is proposed to extend the ZVS operation range on the inverter. In [35], [36], to achieve ZVS operation on both the inverter and the rectifier with a wide range, a Variable-Angle-Phase-Shift (VAPS) modulation method is proposed for regulating the dual-side active bridge converter. However, ZVS operations have been designed for eliminating the turn-on loss of the MOSFETs, and the turn-off loss is always ignored. In fact, the turn-off loss is still significant and occupies a large percentage of the overall power loss [37].

Recently, for the dual-channel power converters, a kind concept of partial power processing (PPP) is proposed [38]-[41]. These channels are divided into the main channel and the auxiliary channel. Generally, only a small part of power flows through the auxiliary channel is processed to adjust the power demands of the load. The main channel operates with nearly no power processing and minimal switching loss. Thus, the overall system efficiency can be effectively improved.

In this paper, to achieve high system efficiency and low power loss at the receiver side, the dual-receiver WPT system with the PPP control method is proposed innovatively. The basic idea is to regulate only one rectifier under different output power conditions. Thus, compared with the conventional power distribution method based on impedance matching, the switching loss in the WPT system with the PPP control method can be reduced apparently, especially in light-load conditions.

The contributions of this paper are listed as follows.

1) Here, the dual-receiver WPT system for LEVs charging is adopted with the PPP control method for the first time. Within the PPP control, only one active rectifier will be regulated by VAPS modulation to adjust the load current requirement, while the other is fixed at a constant conducting angle with a low switching loss. Thus, the total switching loss on the receiver side can be effectively reduced.

2) Under different charging statuses and coupler misalignments, the PPP control method is strictly formulated, considering the load current requirement and the variation of the mutual inductance. By calculating and comparing the switching loss of the MOSFETs, the operation modes of each active rectifier and its boundary conditions are well designed for further reducing the switching loss on active rectifiers and improving the overall system efficiency.

3) Considering the actual application conditions of the WPT system, a closed-loop control strategy, including the hysteresis control and the PI control, is proposed. The hysteresis control is designed for selecting and switching the operation modes of the receiver with seamless transitions, and the PI control is adopted for regulating the system output power with a well dynamic response. Thus, the power transferred from each receiver coil can be dynamically regulated based on the different load power requirements and the misalignment conditions. According to the closed-loop experiment, the apparent efficiency improvement of the system can be achieved.

II. Analysis of the Dual-Receiver WPT System

A. Circuit Description and Analysis

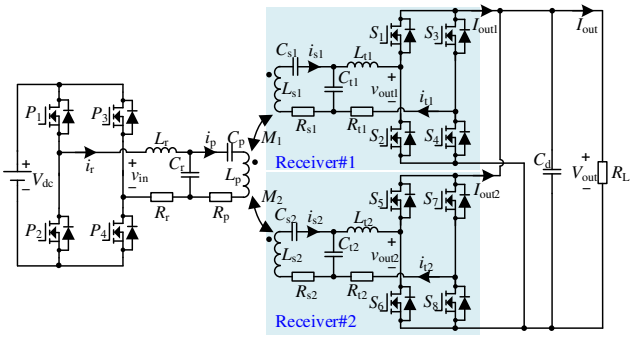

Fig. 1. Schematic diagram of the dual-receiver WPT system with the LCC-LCC compensation networks.

The proposed WPT system is depicted in Fig. 1. The dual-receiver topology is adopted in the receiver for increasing the power transfer capacity and alleviating the current stress. V_{dc} is the DC input voltage, while V_{out} is the DC output voltage on the load resistance R_L. On the transmitter side, a high-frequency inverter (P_1-P_4) and an LCC compensation network are adopted to offer a constant current in the transmitter coil L_p. L_r, C_r, C_p are the compensation elements. On the receiver side, two completely similar receivers, i.e., Receiver #1 and Receiver #2, are employed with two parallel-connected active rectifiers (S_1-S_4, S_5-S_8). L_{s1} and L_{s2} are the two receiver coils. Similarly, L_{t1}, L_{t2}, C_{s1}, C_{t1}, C_{s2}, and C_{t2} form the LCC compensation networks. By designing L_{t1} and L_{t2} in the LCC networks on the receiver side, the current stress of receiver coils can be further reduced. Moreover, M_1 and M_2 are the mutual inductances between the transmitter coil and the two receiver coils. R_r, R_p, R_{s1}, R_{t1}, R_{s2}, and R_{t2} symbolize the ESRs of each loop.

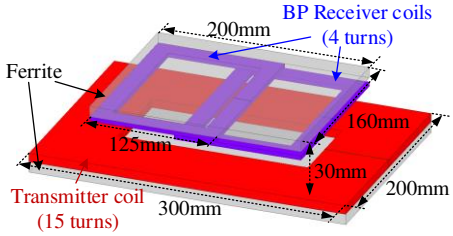

Fig. 2. The model and dimensions of the magnetic coupler.

The magnetic coupler model is designed and shown in Fig. 2. The transmitter coil is square, while the two receiver coils are set as the Bipolar (BP) structure to improve misalignment tolerance with nearly no cross-coupling [13]. By designing the receiver coils with the same shape and size, whether the LEV is misaligned on the left or right, one of the receiver coils can be regarded as the main power channel, and the other is the auxiliary power channel. Thus, the system output power can be ensured in different misalignment conditions.

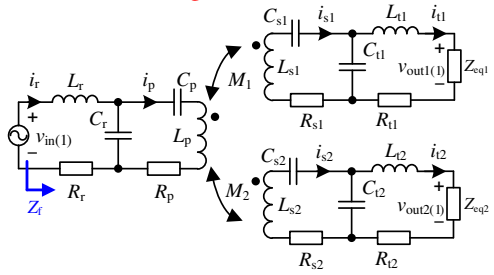

Fig. 3. The equivalent circuit of the proposed WPT system.

The Fundamental Harmonic Approximation (FHA) method is used to analyze the WPT system. The equivalent circuit of the proposed WPT system is depicted in Fig. 3. $v_{in(1)}$ is the fundamental component of the output voltage of the inverter with the operating frequency f, while $v_{out1(1)}$ and $v_{out2(1)}$ are the fundamental components of the input voltage of the active rectifiers. Z_{eq1} and Z_{eq2} are the equivalent load impedances of the two active rectifiers. Z_f is the equivalent reflected impedance at the output side of the inverter.

To ensure the resonance of each current loop, the compensated capacitors can be obtained as

$$\begin{cases} C_r = (\omega^2 L_r)^{-1} & C_p = \left(\omega^2 \left(L_p - L_r\right)\right)^{-1} \\ C_{t1} = (\omega^2 L_{t1})^{-1} & C_{s1} = \left(\omega^2 \left(L_{s1} - L_{t1}\right)\right)^{-1} \\ C_{t2} = (\omega^2 L_{t2})^{-1} & C_{s2} = \left(\omega^2 \left(L_{s2} - L_{t2}\right)\right)^{-1} \end{cases}, \quad (1)$$

where $\omega=2\pi f$ is the operating angular frequency. Based on Kirchhoff's Voltage Law (KVL), while ignoring the ESRs in the circuit, the system can be derived as

$$\begin{cases} \dot{V}_{in(1)} = \left(j\omega L_r + \frac{1}{j\omega C_r}\right)\dot{I}_r - \frac{1}{j\omega C_r}\cdot\dot{I}_p \\ 0 = j\omega M_1 \dot{I}_{s1} + j\omega M_2 \dot{I}_{s2} + \frac{1}{j\omega C_r}\cdot\dot{I}_r + \left(j\omega L_p + \frac{1}{j\omega C_r} + \frac{1}{j\omega C_p}\right)\dot{I}_p \\ 0 = j\omega M_1 \dot{I}_p + \left(j\omega L_{s1} + \frac{1}{j\omega C_{s1}} + \frac{1}{j\omega C_{t1}}\right)\dot{I}_{s1} - \frac{1}{j\omega C_{t1}}\cdot\dot{I}_{t1} \\ 0 = j\omega M_2 \dot{I}_p + \left(j\omega L_{s2} + \frac{1}{j\omega C_{s2}} + \frac{1}{j\omega C_{t2}}\right)\dot{I}_{s2} - \frac{1}{j\omega C_{t2}}\cdot\dot{I}_{t2} \\ \dot{V}_{out1(1)} = \left(j\omega L_{t1} + \frac{1}{j\omega C_{t1}}\right)\dot{I}_{t1} - \frac{1}{j\omega C_{t1}}\cdot\dot{I}_{s1} \\ \dot{V}_{out2(1)} = \left(j\omega L_{t2} + \frac{1}{j\omega C_{t2}}\right)\dot{I}_{t2} - \frac{1}{j\omega C_{t2}}\cdot\dot{I}_{s2} \end{cases}, \quad (2)$$

where

$$\begin{cases} \dot{V}_{out1(1)} = \dot{I}_{t1}\cdot Z_{eq1} \\ \dot{V}_{out2(1)} = \dot{I}_{t2}\cdot Z_{eq2} \end{cases}. \quad (3)$$

Substituting (1) and (3) into (2), the currents in each loop can be obtained as

$$\begin{cases} \dot{I}_r = \dot{V}_{in(1)}\cdot\left(\frac{M_1^2 Z_{eq1}}{\omega^2 L_r^2 L_{t1}^2} + \frac{M_2^2 Z_{eq2}}{\omega^2 L_r^2 L_{t2}^2}\right) & \dot{I}_p = \frac{\dot{V}_{in(1)}}{j\omega L_r} \\ \dot{I}_{s1} = \dot{V}_{in(1)}\cdot\frac{M_1 Z_{eq1}}{\omega^2 L_r L_{t1}^2} & \dot{I}_{t1} = -\dot{V}_{in(1)}\cdot\frac{M_1}{j\omega L_r L_{t1}} \\ \dot{I}_{s2} = \dot{V}_{in(1)}\cdot\frac{M_2 Z_{eq2}}{\omega^2 L_r L_{t2}^2} & \dot{I}_{t2} = -\dot{V}_{in(1)}\cdot\frac{M_2}{j\omega L_r L_{t2}} \end{cases}. \quad (4)$$

Thus, the currents to voltage gain can be given as follows

$$\begin{cases} G_{IV1} = \frac{I_{t1}}{V_{in(1)}} = \frac{M_1}{L_r L_{t1}} \\ G_{IV2} = \frac{I_{t2}}{V_{in(1)}} = \frac{M_2}{L_r L_{t2}} \end{cases}, \quad (5)$$

where I_{t1} and I_{t2} are the Root-Mean-Square (RMS) values of the input currents of the two active rectifiers, and V_{in} is the RMS value of the output voltage of the inverter.

According to (5), since G_{IV1} and G_{IV2} are not related to the load impedance, the adopted LCC-LCC compensation network is therefore ideal to realize the load-independent constant current output characteristic. The load current I_{out} is the sum of the output current of the two rectifiers, which should be defined as

$$I_{out} = I_{out1} + I_{out2}. \quad (6)$$

Meanwhile, the load current I_{out} is also determined by the modulation method and depth of these two active rectifiers.

The load voltage V_{out} and load power P_{out} can be derived as

$$V_{out} = \left(I_{out1} + I_{out2}\right)\cdot R_L, \quad (7)$$

$$P_{out} = \left(I_{out1} + I_{out2}\right)^2 \cdot R_L. \quad (8)$$

In addition, according to (4), the equivalent impedance Z_f reflected on the transmitter side can be solved as

$$Z_f = \frac{\dot{V}_{in(1)}}{\dot{I}_r} = \frac{\omega^2 L_r^2}{\left(\frac{M_1^2}{L_{t1}^2} Z_{eq1} + \frac{M_2^2}{L_{t2}^2} Z_{eq2}\right)}. \quad (9)$$

B. VAPS Modulation Method

When the system operates at the Full-load condition, to ensure enough output power for the load requirement, the duty cycles of the active rectifiers should be 50%. However, when the required load power is reduced caused by the variations of the battery charging conditions, the active rectifiers should be regulated to suit the load demands. The VAPS modulation method utilized here has been proven to regulate the output power while realizing the ZVS operation of the converter [35]. Fig. 4 shows the waveforms of the VAPS method in this paper. The inverter operates at a constant frequency, a fixed duty cycle, and a zero phase-shift angle. Thus, the fundamental component of the output voltage of the inverter can be expressed as

$$V_{in(1)} = 2\sqrt{2}V_{dc}/\pi. \quad (10)$$

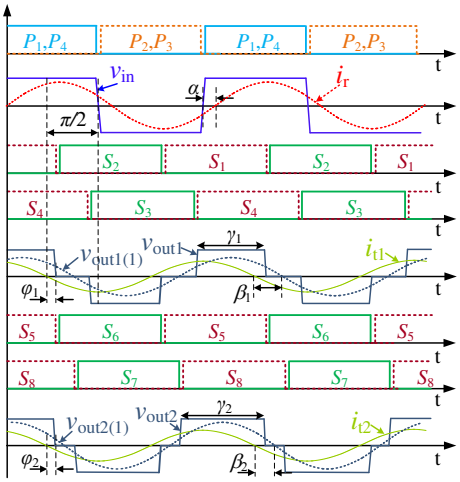

Fig. 4. Waveforms of VAPS control of the WPT system.

For the WPT system with the VAPS control, adjusting the conducting angle of the active rectifier γ_1 (γ_2) and the phase difference between the input current and voltage of the rectifier β_1 (β_2) is available to regulate the system output power. φ_1 (φ_2) is the phase difference between the positive-to-negative zero-crossing point of i_{t1} (i_{t2}) and S_1 (S_5), which is always expected to be a tiny positive value to ensure the ZVS operation of all MOSFETs in rectifiers. γ_1 (γ_2) and β_1 (β_2) should satisfy

$$\begin{cases} \beta_1 = \varphi_1 + \frac{\pi-\gamma_1}{2} > \frac{\pi-\gamma_1}{2} \\ \beta_2 = \varphi_2 + \frac{\pi-\gamma_2}{2} > \frac{\pi-\gamma_2}{2} \end{cases}. \quad (11)$$

For the sake of analysis, Receiver #1 is picked up for analyzing the circuit model of the receiver side as an example since

the operation principles of both receivers are the same. The output voltage and current of the rectifier can be derived as

$$V_{\text{out1(1)}} = \frac{2\sqrt{2}}{\pi} V_{\text{out}} \sin\left(\frac{\gamma_1}{2}\right), \tag{12}$$

$$I_{\text{out1}} = \frac{2\sqrt{2}}{\pi} \cdot \left(\sin\left(\frac{\gamma_1}{2}\right) \cdot \cos\left(\frac{\pi-\gamma_1}{2}+\varphi_1\right)\right) \cdot I_{\text{t1}}. \tag{13}$$

According to (12) and (13), the conducting angle γ_1 can be derived as

$$\gamma_1 = \varphi_1 + \arccos\left(\cos(\varphi_1) - \frac{\sqrt{2}\pi I_{\text{out1}}}{2I_{\text{t1}}}\right). \tag{14}$$

Substituting (4), (10) and (12) into (3), the equivalent impedance Z_{eq1} can be derived as

$$Z_{\text{eq1}} = \frac{\dot{V}_{\text{out1(1)}}}{\dot{I}_{\text{t1}}} = \frac{\omega L_{\text{r}} L_{\text{t1}} V_{\text{out}}}{V_{\text{dc}} M_1} \cdot \sin\left(\frac{\gamma_1}{2}\right) \cdot \left(\cos(\beta_1) + j \cdot \sin(\beta_1)\right). \tag{15}$$

Then, according to (4) and (15), the RMS value of the current in the receiver coil I_{s1} can be derived as

$$I_{\text{s1}} = \frac{2\sqrt{2}V_{\text{out}}}{\pi\omega L_{\text{t1}}} \sin\left(\frac{\gamma_1}{2}\right). \tag{16}$$

Besides, according to the waveforms in Fig. 4, it is evident that only S_1 and S_2 can turn off at a nearly zero current, and the turn-off current of S_3 and S_4 are still large. Here, the turn-off loss of the MOSFET can be regarded to be proportional to the turn-off current. Thus, though the ZVS operation can be achieved in the rectifiers with the VAPS modulation method, the turn-off losses still take large parts of the overall power loss, especially with the high operating frequency. TABLE I shows the turn-off angles of the rectifier. Since φ_1 (φ_2) is a constant tiny positive angle, the turn-off loss is mainly determined by the conducting angle γ_1 (γ_2).

TABLE I
THE TURN-OFF ANGLES OF THE MOSFETS IN RECEIVER #1

	S_1	S_2	S_3	S_4
turn-off angle	φ_1	φ_1	$\varphi_1+\pi-\gamma_1$	$\varphi_1+\pi-\gamma_1$

C. Conventional Power Distribution Method Based on Impedance Matching

Due to the merits of the LCC-LCC compensation networks and the BP coil structure, the transferred power of each receiver can be regulated individually. The circulation phenomenon, which seriously harms the system output power and the overall efficiency, is suppressed even in severe misalignment conditions. However, in the whole charging process of vehicle batteries, the variation range of the load resistance is extensive. In the dual-receiver WPT system, for the same P_{out}, there will be many different power distribution schemes between the two receivers. Here, to reduce the power loss at the receiver side, including the ESRs loss and the rectifier loss, the optimal power distribution scheme should be figured out.

In the WPT systems with multi-transmitters (receivers), the power distribution methods based on impedance matching have been already proposed [25]-[28]. Whether the mutual inductances between the transmitter coils and receiver coils are balanced or not, the same current in each coil is always expected. The output current distribution with the conventional power distribution method is given in Fig. 5.

For the sake of analysis, it is assumed that $M_1 \le M_2$. Besides, to achieve the ZVS operation in both rectifiers, here φ_1 and φ_2 are set as a constant value φ and define $\lambda = \frac{2\sqrt{2}}{\pi}\cos(\varphi)$.

1) M_1=M_2 with the conventional power distribution method

As shown in Fig. 5(a), when M_1=M_2, the rectifiers are regulated to output the same current, i.e., I_{out1}=I_{out2} and γ_1=γ_2. According to (6) and (13), the system output current meets

$$\begin{aligned} I_{\text{out}} &= \frac{4\sqrt{2}}{\pi} \cdot \left(\sin\left(\frac{\gamma_1}{2}\right) \cdot \cos\left(\frac{\pi-\gamma_1}{2}+\varphi\right)\right) \cdot I_{\text{t1}} \\ &= \frac{4\sqrt{2}}{\pi} \cdot \left(\sin\left(\frac{\gamma_2}{2}\right) \cdot \cos\left(\frac{\pi-\gamma_2}{2}+\varphi\right)\right) \cdot I_{\text{t2}} \end{aligned}. \tag{17}$$

Thus, the switching losses of the rectifiers are totally the same.

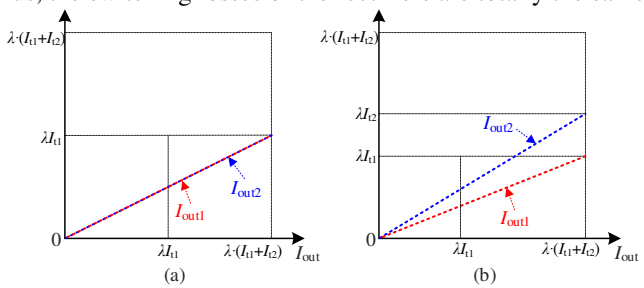

Fig. 5. I_{out1} and I_{out2} against I_{out} with the conventional power distribution method when (a) M_1=M_2 and (b) M_1<M_2.

2) M_1<M_2 with the conventional power distribution method

To minimize the ESRs losses of the receiver coils, with the conventional power distribution method, I_{s1} and I_{s2} are always regulated as the same value. According to (13), when M_1<M_2, to ensure the balance between I_{s1} and I_{s2}, γ_1=γ_2 is also necessary since L_{t1}=L_{t2}. Thus, as shown in Fig. 5(b), the ratio of I_{out1} and I_{out2} is the same as the ratio of I_{t1} and I_{t2}. The system output current meets

$$\begin{aligned} I_{\text{out}} &= \frac{2\sqrt{2}}{\pi} \cdot \left(\sin\left(\frac{\gamma_1}{2}\right) \cdot \cos\left(\frac{\pi-\gamma_1}{2}+\varphi\right)\right) \cdot \left(I_{\text{t1}} + I_{\text{t2}}\right) \\ &= \frac{2\sqrt{2}}{\pi} \cdot \left(\sin\left(\frac{\gamma_2}{2}\right) \cdot \cos\left(\frac{\pi-\gamma_2}{2}+\varphi\right)\right) \cdot \left(I_{\text{t1}} + I_{\text{t2}}\right) \end{aligned}. \tag{18}$$

Moreover, according to (9) and (15), the reflected impedance Z_{f} can be derived as

$$Z_{\text{f}} = \frac{\omega L_{\text{r}} V_{\text{dc}}}{\left(\frac{M_1}{L_{\text{t1}}} \cdot \sin\left(\frac{\gamma_1}{2}\right) \cdot \left(\cos(\beta_1) + j \cdot \sin(\beta_1)\right) + \frac{M_2}{L_{\text{t2}}} \cdot \sin\left(\frac{\gamma_2}{2}\right) \cdot \left(\cos(\beta_2) + j \cdot \sin(\beta_2)\right)\right) \cdot V_{\text{out}}}. \tag{19}$$

D. Power Loss Calculation

To clarify the main factors affecting the overall power loss, the power loss model is established and analyzed as follow.

1) ESRs loss:

The ESRs loss consists of the power loss on the inductors, coils and the compensated capacitors, which can be derived as

$$\begin{aligned} P_{\text{ESRs}} &= P_{\text{ESRs\_rec}} + P_{\text{ESRs\_tran}} \\ &= I_{\text{s1}}^2 R_{\text{s1}} + I_{\text{s2}}^2 R_{\text{s2}} + I_{\text{t1}}^2 R_{\text{t1}} + I_{\text{t2}}^2 R_{\text{t2}} + I_{\text{r}}^2 R_{\text{r}} + I_{\text{p}}^2 R_{\text{p}} \end{aligned}, \tag{20}$$

where $P_{\text{ESRs\_rec}}$ and $P_{\text{ESRs\_tran}}$ indicate the ESRs losses in the receiver side and the transmitter side.

2) Active rectifiers loss:

The power loss on the active receivers P_{rec} can be delivered into the conducting loss and the switching loss, i.e.,

$$P_{rec} = P_{rec\_cond} + P_{rec\_sw} . \quad (21)$$

where P_{rec_cond} presents the conducting loss of the MOSFETs in rectifiers, and P_{rec_sw} presents its switching loss. Ignoring the conducting loss on the anti-paralleled diodes of the MOSFETs as it only accounts for a tiny part of P_{rec}, P_{rec_cond} can be expressed as

$$P_{rec\_cond} = 2\cdot\left(I_{t1}^2 + I_{t2}^2\right)\cdot R_{rec\_sd}, \quad (22)$$

where R_{rec_sd} is the conducting resistance of the MOSFETs in the rectifier, which can be found or fitted from the datasheet of the MOSFET. Meanwhile, with the VAPS modulation method, P_{rec_sw} can be expressed as [42], [43]

$$P_{rec\_sw} = 2\sqrt{2}\left(A_{rec} + B_{rec}\right)V_{out} f \cdot \begin{pmatrix} I_{t1}\cdot\left(\left|\sin(\varphi_1)\right| + \left|\sin(\varphi_1 + \pi - \gamma_1)\right|\right) \\ + I_{t2}\cdot\left(\left|\sin(\varphi_2)\right| + \left|\sin(\varphi_2 + \pi - \gamma_2)\right|\right) \end{pmatrix}, \quad (23)$$

where A_{rec}=E_{rec_off}/($U_{rec\_DD}I_{rec\_D}$) indicates the value of the turn-off energy of the MOSFETs in the rectifier at the standard test condition, and B_{rec}=Q_{rec_DD}/I_{rec_RD} indicates the value of the switching loss of the anti-paralleled diodes. E_{rec_off}, U_{rec_DD}, I_{rec_D}, Q_{rec_DD}, and I_{rec_RD} can be found in the datasheet or tested/modelled by the users. The modelling and calculating methods have been already introduced in [37] and [44]. Although the calculated switching loss cannot be completely accurate, the results still have a substantial reference value.

3) Inverter loss:

The inverter loss can also be expressed as

$$P_{inv} = P_{inv\_cond} + P_{inv\_sw}, \quad (24)$$

where the conducting loss P_{inv_cond} and the switching loss P_{inv_sw} can be expressed as

$$P_{inv\_cond} = 2\cdot I_r^2\cdot R_{inv\_ds}, \quad (25)$$

$$P_{inv\_sw} = 4\sqrt{2}\left(A_{inv} + B_{inv}\right)V_{dc} I_r f\left|\sin(\alpha)\right| . \quad (26)$$

where A_{inv}=E_{inv_off}/($U_{inv\_DD}I_{inv\_D}$) and B_{inv}=Q_{inv_DD}/I_{inv_RD} indicate the corresponding turn-off loss in the inverter. Similarly, R_{inv_ds}, E_{inv_off}, U_{inv_DD}, I_{inv_D}, Q_{inv_DD}, and I_{inv_RD} can be found in the datasheet or tested/modelled by the users. Here, α is the phase difference between $v_{in(1)}$ and i_r, which can be defined as

$$\alpha = \arctan\left(\frac{\mathrm{Im}(Z_f)}{\mathrm{Re}(Z_f)}\right). \quad (27)$$

III. Proposed PPP Based Power Distribution Method

With the conventional power distribution scheme based on impedance matching, the receiver coil losses can be minimized. However, by designing the circuit structure and its parameters, the receiver coil losses can be limited at a low level. Meanwhile, to release the conducting loss of the rectifier, the low-conducting-resistance MOSFETs is always expected in the high-current output WPT systems. Nevertheless, this kind of MOSFETs always performs poor in the switching speed. While regulating the system output power by adjusting the conducting angle of the rectifiers, the switching losses of the rectifiers account for the majority of the power loss at the receiver side, even in the ZVS conditions.

A. Principle of the PPP Control with VAPS Modulation

There are three statuses for the active rectifiers, and the waveforms of each status are given in Fig. 6. With the Shutting status in Fig. 6(a), only the low-side MOSFETs, i.e., S_2 (S_6) and S_4 (S_8), are continuously conducting. Thus, v_{out1} (v_{out2}) and the output power of the rectifier are zero. In this situation, the switching loss of the rectifier can be ignored since there is no switching operation. While the rectifier is regulated by VAPS modulation and γ_1 (γ_2) is less than π, as shown in Fig. 6(b), I_{out1} (I_{out2}) is determined by γ_1 (γ_2). Meanwhile, according to (23), the turn-off loss of the rectifier should be taken into account even the ZVS operation is achieved. While γ_1 (γ_2) reaches π, which can be regarded as the Full-load status in Fig. 6(c), the rectifier will operate with its maximum output current. Then the switching loss of the rectifier is limited since the turn-off currents are nearly zero when MOSFETs turn off.

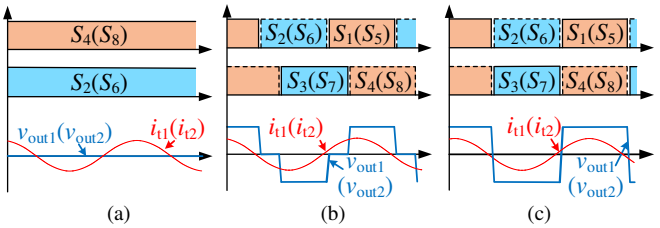

Fig. 6. Waveforms of the rectifiers with (a) Shutting status, (b) VAPS modulation, and (c) Full-load status.

Obviously, to decrease the switching losses of the rectifiers, adjusting the output current of only one rectifier while keeping the other in Shutting or Full-load status is a workable way. Based on this idea, the PPP control method for the WPT system is proposed in this work. According to the system required output current, the operation modes of the receiver can be divided into the following four modes, as shown in TABLE II.

TABLE II
Operation Modes of the Rectifiers in Four Modes

Operation mode	The status of Receiver #1	The status of Receiver #2
Mode 1	VAPS	Shutting
Mode 2	Shutting	VAPS
Mode 3	Full-load	VAPS
Mode 4	VAPS	Full-load

Here, only one rectifier will be modulated by the VAPS method to adjust the output power dynamically. The other rectifier will operate at the Full-load status with a low turn-off current or shut down with no switching operating. Since the switching loss of a single MOSFET can be regarded to be proportional to its turn-off current, the switching loss on the rectifier with Full-load or Shutting mode can be well limited. Besides, with the unbalanced M_1 and M_2, the PPP method must be adjusted to suit different misalignment conditions.

According to the analysis of the turn-off current and the receiver operation mode, the trends of total switching loss on the active rectifiers P_{rec_sw} with different operation modes against the output current I_{out} are plotted in Fig. 7. When M_1=M_2, the results of the two groups (Mode 1=Mode 2, Mode 3 =Mode 4) are the same. Therefore, the operation of the rectifiers can be divided into two modes with the variation of I_{out}. According to (13) and (23), the trend of P_{rec_sw} against I_{out} is plotted as the solid green curve in Fig. 7(a). Besides, when M_1≠M_2, the operation of the rectifiers will be divided into four modes. Since

there are overlaps between the four operation modes, the one with lower P_{rec_sw} should be picked up as the selected operation mode. By combining the curve of the selected operation modes, the final trend of P_{rec_sw} is also plotted as the solid green curve in Fig. 7(b).

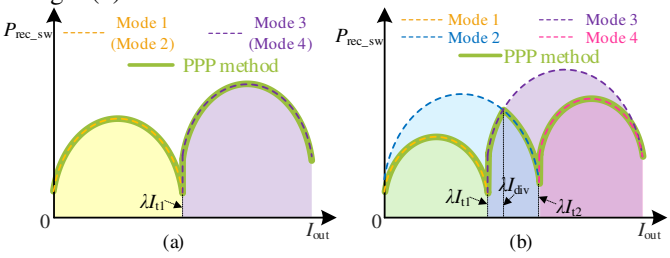

Fig. 7. The total switching loss on the active rectifiers P_{rec_sw} against I_{out} when (a) M_1=M_2 and (b) M_1<M_2.

B. Power Distribution Scheme of the PPP Control

Based on the selected operation modes, the distribution scheme of rectifier output currents with the PPP control method is depicted in Fig. 8.

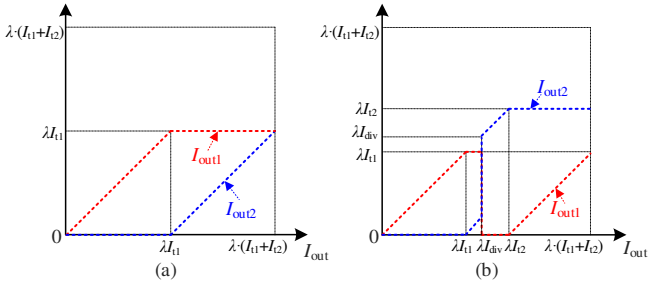

Fig. 8. The output current I_{out1} and I_{out2} against I_{out} with the proposed PPP control method when (a) M_1=M_2 and (b) M_1<M_2.

1) M_1=M_2 with the PPP method

The trends of I_{out1} and I_{out2} against I_{out} with the proposed PPP control method when M_1=M_2 are shown in Fig. 8(a). To release P_{rec_sw}, when $I_{out}\le\lambda I_{t1}$, only γ_1 is adjusted, and Receiver #2 is shut down with no switching loss, i.e.,

$$\begin{cases} I_{out1}=I_{out}=\dfrac{2\sqrt{2}}{\pi}\cdot\left(\sin\left(\dfrac{\gamma_1}{2}\right)\cdot\cos\left(\dfrac{\pi-\gamma_1}{2}+\varphi\right)\right)\cdot I_{t1} \\ I_{out2}=0 \end{cases}. \quad (28)$$

While $I_{out}>\lambda I_{t1}$, γ_1 is fixed at π, and the rectifier in Receiver #2 is adjusted to suit the rest of the load required current, i.e.,

$$\begin{cases} I_{out1}=\dfrac{2\sqrt{2}}{\pi}\cdot\cos(\varphi)\cdot I_{t1} \\ I_{out2}=I_{out}-I_{out1}=\dfrac{2\sqrt{2}}{\pi}\cdot\left(\sin\left(\dfrac{\gamma_2}{2}\right)\cdot\cos\left(\dfrac{\pi-\gamma_2}{2}+\varphi\right)\right)\cdot I_{t2} \end{cases}. \quad (29)$$

Thus, in each operating condition, only one rectifier is dynamically adjusted with limited switching loss, while the other rectifier could operate with nearly no switching loss.

2) M_1<M_2 with PPP method

Moreover, if M_1 and M_2 are unbalanced, the power distribution method should consider not only the total switching loss on the rectifiers but also the capacity of the output current from the single rectifier. While M_1<M_2, the trends of I_{out1} and I_{out2} against I_{out} are shown in Fig. 8(b). When $I_{out}\le\lambda I_{t1}$, similarly, only γ_1 is adjusted, and Receiver #2 is shut down, i.e., the receiver operates in Mode 1. The output current of each receiver meets (28).

When λI_{t1}<$I_{out}\le\lambda I_{t2}$, there are two possible operation modes of the receiver. Cause the output current of Receiver #1 cannot ever satisfy the required power, Receiver #2 must be utilized for power transmission individually or cooperatively. To choose the more suitable operation mode, I_{div} is defined as the boundary line of this load range and can be calculated by comparing the switching losses of Mode 2 and Mode 3.

While λI_{t1}<$I_{out}\le\lambda I_{div}$, by comparing the switching losses of the possible operation modes, γ_1 should still be fixed at π, and γ_2 is adjusted to suit the rest of the load required current, which indicates that the receiver operates in Mode 3. The output current of each receiver meets (29). While λI_{div}<$I_{out}\le\lambda I_{t2}$, only γ_2 is adjusted, and Receiver #1 is shut down with no switching loss. In this case, the receiver operates in Mode 2, i.e.,

$$\begin{cases} I_{out1}=0 \\ I_{out2}=I_{out}=\dfrac{2\sqrt{2}}{\pi}\cdot\left(\sin\left(\dfrac{\gamma_2}{2}\right)\cdot\cos\left(\dfrac{\pi-\gamma_2}{2}+\varphi\right)\right)\cdot I_{t2} \end{cases}. \quad (30)$$

Additionally, when $I_{out}>\lambda I_{t2}$, to ensure the required power, γ_2 is still fixed at π, and γ_1 is adjusted to suit the rest of the load required current. Here, the receiver operates in Mode 4, i.e.,

$$\begin{cases} I_{out1}=I_{out}-I_{out2}=\dfrac{2\sqrt{2}}{\pi}\cdot\left(\sin\left(\dfrac{\gamma_1}{2}\right)\cdot\cos\left(\dfrac{\pi-\gamma_1}{2}+\varphi\right)\right)\cdot I_{t1} \\ I_{out2}=\dfrac{2\sqrt{2}}{\pi}\cdot\cos(\varphi)\cdot I_{t2} \end{cases}. \quad (31)$$

C. The Power Loss Analysis and Comparison

To verify the effect of the proposed PPP control on the efficiency improvement in the dual-receiver WPT system, analysis and comparison of the power loss in each part are necessary. The corresponding mathematical model has been introduced in Section II, and the system parameters are list in TABLE III.

TABLE III
SYSTEM SPECIFICATION AND PARAMETER VALUES

Symbol	*Value*	*Symbol*	*Value*	*Symbol*	*Value*
V_{dc}	350V	V_{out}	24V	I_{out}	5~50A
L_r	29.5uH	C_r	21.46nF	R_r	40mΩ
L_p	90.4uH	C_p	10.4nF	R_p	220.1mΩ
L_{t1}	2.63uH	C_{t1}	240.8nF	R_{t1}	2.9mΩ
L_{t2}	2.64uH	C_{t2}	239.9nF	R_{t2}	2.9mΩ
L_{s1}	6.92uH	C_{s1}	147.6nF	R_{s1}	23.0mΩ
L_{s2}	7.09uH	C_{s2}	142.3nF	R_{s2}	24.1mΩ
f	200kHz	S_1-S_8	IXFX420N10T	A_{rec}+ B_{rec}	138ns
Air gap	30mm	P_1-P_4	C3M0021120D	A_{inv}+ B_{inv}	34.2ns

According to the system circuit and power loss analysis below, the theoretical power loss comparison is shown in Fig. 9. The rectifier switching loss P_{rec_sw} with the conventional power distribution method under different ratios of M_1 to M_2 and I_{out} is shown in Fig. 9(a). Here, P_{rec_sw} is independent of M_1/M_2 and is affected by I_{out}. While the system is controlled by the PPP method, as shown in Fig. 9(b), P_{rec_sw} is well limited since only one rectifier is dynamically regulated, and the other rectifier operates with a tiny turn-off current or even be shut down. This result is consistent with the theoretical analysis.

Meanwhile, the ESRs loss at the receiver side P_{ESRs_rec} and the rectifier conducting loss P_{rec_cond} with these two power distribution methods are plotted in Fig. 9(c) and (d). With the low ESRs of the receiver coils in the small size magnetic coupler and the designed compensation parameters, P_{ESRs_rec} is well limited. In theory, though the PPP control method will increase P_{ESRs_rec}, this part of power loss is still a tiny part of the overall system power loss. Meanwhile, by utilizing the IXFX420N10T

in the rectifier, the rectifier conducting loss P_{rec_cond} is also kept at a low level. What needs to be emphasized is that P_{ESRs_rec} and P_{rec_cond} of the system adopting these two power distribution methods have nearly no difference. Thus, while P_{rec_sw} is reduced, the improvement of the system efficiency is significant.

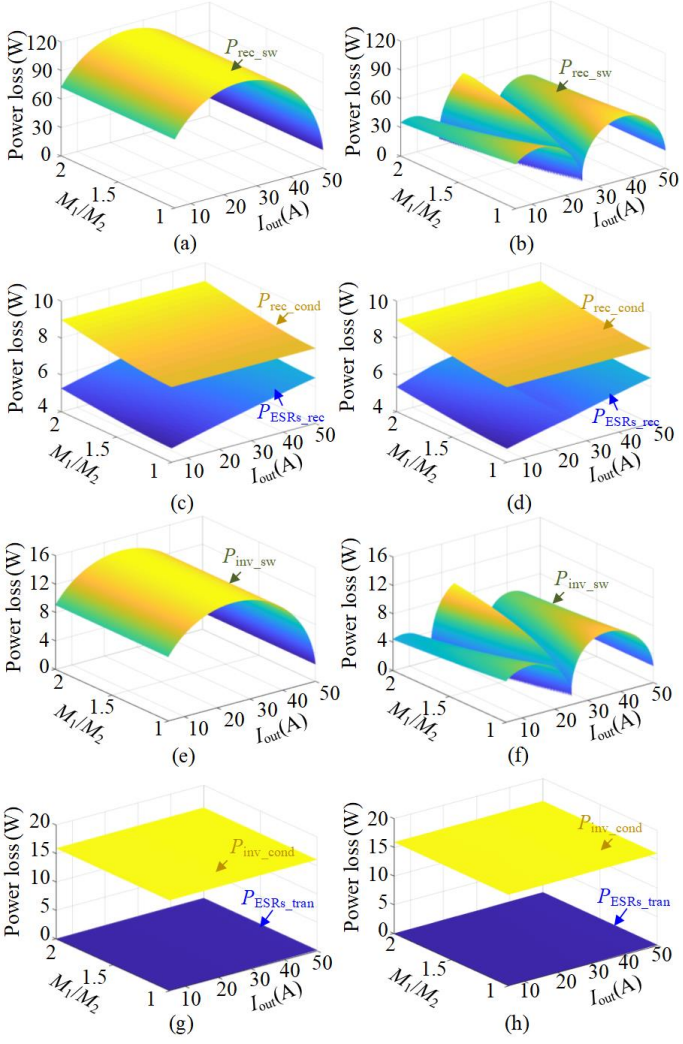

Fig. 9. The calculated power loss of each part. (a) P_{rec_sw} with the conventional power distribution method and (b) the proposed PPP control method, (c) P_{rec_cond} and P_{ESRs_rec} with the conventional power distribution method and (d) the proposed PPP control method, (e) P_{inv_sw} with the conventional power distribution method and (f) the proposed PPP control method, (g) P_{inv_cond} and P_{ESRs_tran} with the conventional power distribution method and (h) the proposed PPP control method.

The switching losses of the inverter with different power distribution methods are plotted in Fig. 9(e) and (f). The curves of P_{inv_sw} have similar trends of P_{rec_sw}, which indicates the effectiveness of the proposed PPP control for reducing the inverter switching loss. Here, by utilizing C3M0021120D in the inverter, P_{inv_sw} accounts for a limited part of the overall system loss. The comparisons of P_{inv_cond} and P_{ESRs_tran} are shown in Fig. 9(g) and (h). Similarly, P_{inv_cond} and P_{ESRs_tran} of the system adopting these two power distribution methods have nearly no difference and occupy a small percentage of the overall system power loss.

D. The Control Strategy and the Diagram of the PPP control

The control diagram of the receiver side is depicted in Fig. 10. The main control goal is to provide the required power depending on the charging state of the vehicle battery. Meanwhile, the ZVS operation should also be realized by the phase tracking modules. Within the control goals, the flowchart of the proposed PPP control is designed in Fig. 11.

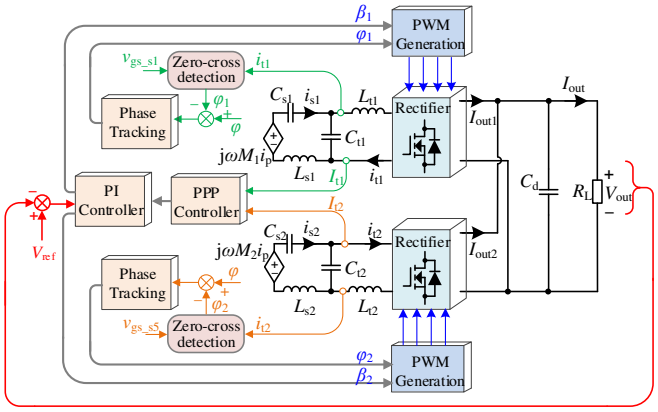

Fig. 10. The control diagram of the PPP-based controller on the receiver side.

Firstly, while I_{t1} and I_{t2} are measured and input to the PPP controller, the boundary lines of the different operation modes can be obtained. Meanwhile, the system output current I_{out} can be calculated with the known β_1 and β_2. By comparing the I_{out}, I_{t1}, I_{t2} and the calculated I_{div}, the receiver operation mode can be selected with hysteresis control in the PPP controller. Only one active rectifier will be dynamically adjusted by the PI controller with the measured V_{out} and the reference output V_{ref}, while the other is fixed with a constant conducting angle π or 0. Secondly, the phases of i_{t1} and i_{t2} are obtained by using zero-cross detection. With the assistance of the phase comparison circuits, phase differences φ_1 and φ_2 are controlled to track the reference angle φ. Thus, the ZVS operations can be guaranteed. By testing the switching performance of the MOSFETs under the whole power range, φ is set as 5° here as an example.

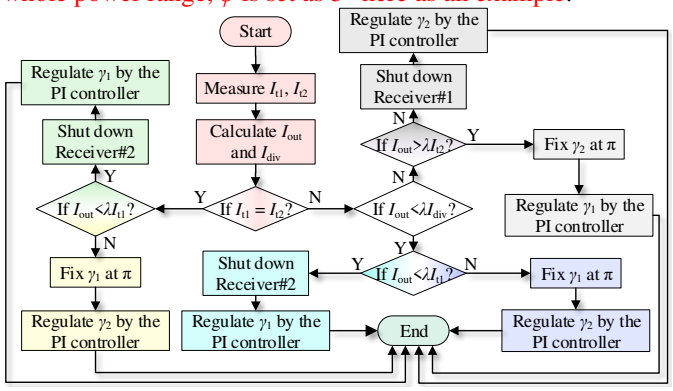

Fig. 11. The flowchart of the PPP-based power distribution strategy.

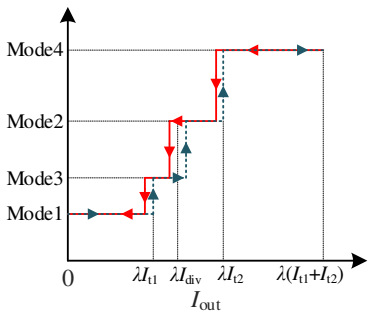

Fig. 12. The diagram of the designed hysteresis control in the PPP controller.

Moreover, to determine and transit the operation modes, considering the characteristics of Mode 1~Mode 4, an available

but straightforward hysteresis control method is designed in the PPP controller. As shown in Fig. 12, due to the output current limitation in Mode 1 and Mode 2, when I_{out} increased to λI_{t1} (λI_{t2}), Receiver #1 (Receiver #2) is not able to provide more power. Thus, the receiver should be switched to Mode 3 (Mode 4) at $I_{out}=\lambda I_{t1}$ ($I_{out}=\lambda I_{t2}$). However, according to the experimental test, when the receiver operation mode switches from Mode 3 (Mode 4) to Mode 1 (Mode 2), the hysteresis switching point is set at $I_{out}=0.98\cdot\lambda I_{t1}$ ($I_{out}=0.98\cdot\lambda I_{t2}$). Besides, since there is a large overlap in the power coverage of Mode 3 and Mode 2, the switching point of Mode 3 to Mode 2 can be set at $I_{out}=1.02\lambda I_{div}$, while the other switching point of Mode 2 to Mode 3 is designed at $I_{out}=0.98\lambda I_{div}$.

IV. Experimental Verifications

A. Experimental Prototype

To verify the validity of the proposed PPP method, a 24V-50A output experimental prototype is built and shown in Fig. 13, using the parameters in TABLE III. Digital signal processor (TMS320F28335) is used as the controller for PWM generation in the proposed control method.

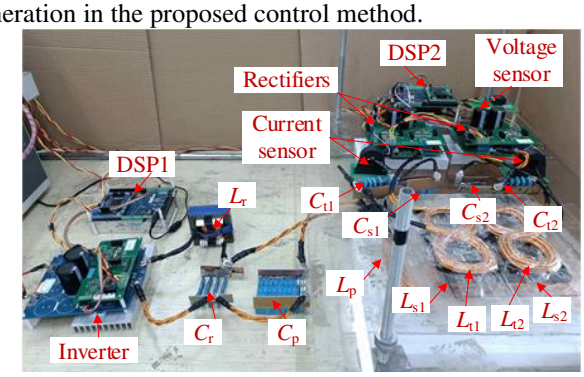

Fig. 13. Experimental setup.

The magnetic coupler with the BP receiver coil structure is employed in this experimental prototype. The dimensions of the magnetic coupler are designed with ANSYS MAXWELL software, as shown in Fig. 2. The simulated and experimental mutual inductances M_1 and M_2 versus x-axis misalignment are shown in Fig. 14. Errors of M_1 and M_2 between the simulation and experiment are subsistent and acceptable, which is caused by the difference between the handmade magnetic coupler and the ideal MAXWELL model. While the magnetic coupler is well-aligned, the coupling coefficient between the single receiver coil and the transmitter coil is about 0.35. $x\in$[-60mm, 60mm] is set as the movement range of the receiver coils.

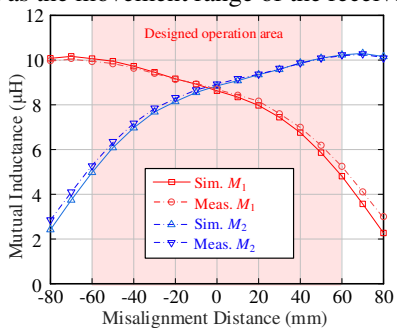

Fig. 14. Simulated and measured M_1 and M_2 against the misalignment distance.

The coils in the experimental setup are shown in Fig. 15. The 20mm^2-Litz-wire is utilized here. In Fig. 15(a), the transmitter coil is made by the two-strand paralleled Litz-wire. For the BP receiver coils, the single-strand Litz-wire is adopted for releasing the weight of the receiver coil since its maximum current is limited in 7A, as shown in Fig. 15(b). It should be noted that, for further reducing the size and weight of the receiver, refer to the inductor integration methods in [45]-[47], the compensation inductors L_{t1} and L_{t2} are integrated at the outside of the ferrite in the receiver. By designing these inductors in the DD structure, these inductors are well decoupled to the receiver coils and the transmitter coil. Then, the load-independent constant output current is still achieved. Meanwhile, since L_{t1} and L_{t2} are only ~2.64uH, the cost of the Litz-wire is also limited even the inductors are made by the two-strand paralleled Litz-wire, as shown in Fig. 15(c).

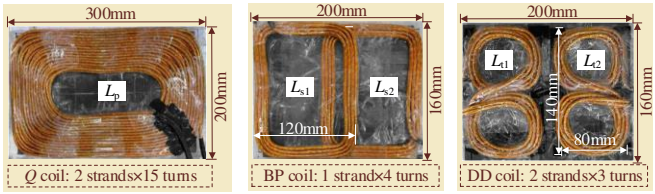

Fig. 15. Structure and dimensions of (a) the transmitter coil, (b) the BP receiver coils and (c) the DD comparison inductors.

B. Experimental Waveforms

1) Waveforms of $M_1=M_2$

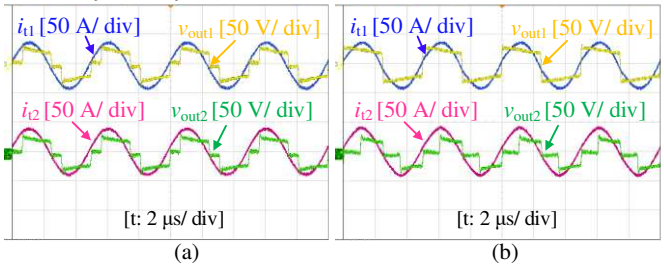

Fig. 16. Experimental waveforms of i_{t1}, i_{t2}, v_{out1}, v_{out2} with (a) the conventional method and (b) the PPP control method when $M_1=M_2$ and I_{out}=37.5A.

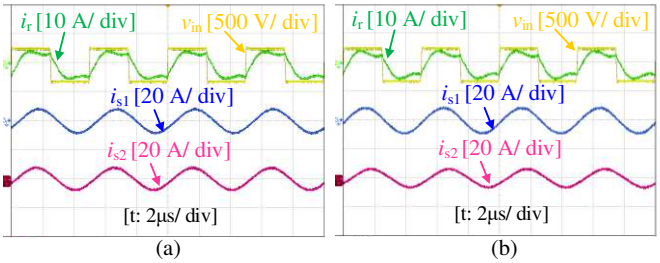

Fig. 17. Experimental waveforms of i_r, i_{s1}, i_{s2}, v_{in} with (a) conventional method and (b) the PPP control method when $M_1=M_2$ and I_{out}=37.5A.

Fig. 16 shows the waveforms of i_{t1}, i_{t2}, v_{out1}, v_{out2} using two different power distribution methods in the heavy-load condition ($I_{out}>\lambda I_{t1}$) with $M_1=M_2$=8.7μH. The DC output voltage and current are maintained at 24V and 37.5A. In Fig. 16(a), when the conventional power distribution method is applied, rectifiers are regulated to output the same i_{t1} and i_{t2} with the $\gamma_1=\gamma_2$. Fig. 16(b) shows the corresponding waveforms with the proposed PPP control method. In this case, Receiver #1 is in Full-load status with $\gamma_1=\pi$, and only the rectifier in Receiver #2 is adjusted to suit the load required current.

Fig. 17 compares the waveforms of i_r, i_{s1}, i_{s2}, v_{in} using two control methods. When the conventional power distribution method is adopted, I_{s1} and I_{s2} are the same, which leads to minimal ESRs loss on the receive coils. While using the PPP

control method, with the rectifiers operating in Mode 3, I_{s2} is lower than I_{s1}. Thus, though the ZVS operation is achieved with both power distribution methods, the measured overall efficiency using the PPP method is up to 87.5%, which is improved by 1.3% compared with that of the conventional method.

Similarly, Fig. 18 contrasts i_{t1}, i_{t2}, v_{out1}, v_{out2} using two methods in light-load condition ($I_{out}\leq\lambda I_{t1}$) with M_1=M_2=8.7μH. The DC output voltage and current are maintained at 24V and 18.5A. Comparing the waveforms in Fig. 16(a) and Fig. 18(a), when using the conventional power distribution method, conducting angles in the light-load condition are smaller, resulting in more switching loss. The measured overall efficiency is sharply decreased from 86.2% to 72.1%. Fig. 18(b) shows the corresponding waveforms with the proposed PPP control method. In this case, only Receiver #2 is adjusted to regulate the system output current, while Receiver #1 is shut to avoid extra switching loss.

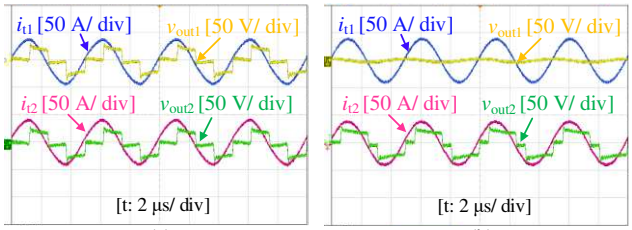

Fig. 18. Experimental waveforms of i_{t1}, i_{t2}, v_{out1}, v_{out2} with (a) the conventional method and (b) the PPP method when M_1=M_2 and I_{out}=18.5A.

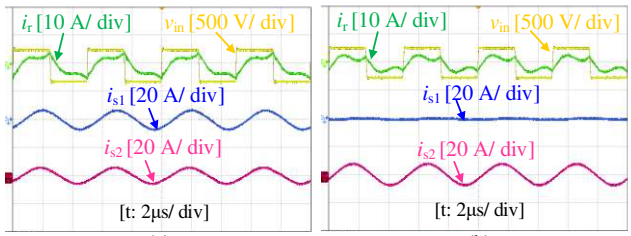

Fig. 19. Experimental waveforms of i_r, i_{s1}, i_{s2}, v_{in} with (a) the conventional method and (b) the proposed PPP control method when M_1=M_2 and I_{out}=18.5A.

As shown in Fig. 19(a), when the conventional power distribution method is adopted, I_{s1} and I_{s2} are still the same. With the PPP control method, I_{s1} is approximately equal to zero, which verifies the theoretical analysis. Besides, as shown in Fig. 19(b), the reactive component and harmonic content in i_r with the PPP method are less than that with the conventional method, which reduces the turn-off loss of the inverter. The measured overall efficiency using the PPP method is up to 79.3%, which is improved by 7.2% compared with the conventional method.

2) Waveforms of M_1<M_2

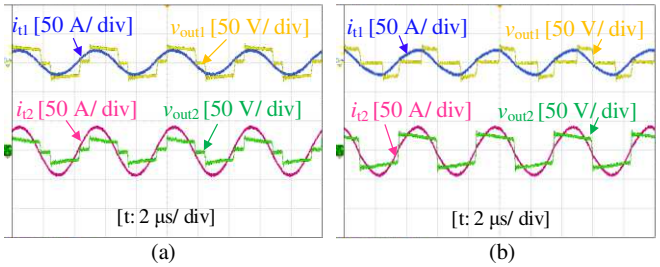

Fig. 20. Experimental waveforms of i_{t1}, i_{t2}, v_{out1}, v_{out2} with (a) conventional method and (b) the PPP control method when M_1=0.5·M_2 and I_{out}=30A.

When M_1=0.5·M_2 (M_1=~5uH and M_2=~10uH), the waveforms of the i_{t1}, i_{t2}, v_{out1}, v_{out2} using the conventional power distribution method are shown in Fig. 20(a). V_{out} and I_{out} are set as 24V and 30A. In this situation, rectifiers are still regulated with γ_1=γ_2 while i_{t1} is only two-thirds as i_{t2}, which results in high switching loss. Here, the measured system efficiency is 86.5%. While using the proposed PPP control method with Mode 4 under the same condition, only γ_1 is adjusted to suit the load requirements, and γ_2 is still fixed at π, as shown in Fig. 20(b). The measured overall efficiency is up to 89.6%, which is improved by 0.9% compared with the conventional method.

Moreover, with the PPP control method, the drain-source voltage and the gate-source voltage of the MOSFET S_1 in the rectifier and the MOSFET P_1 in the inverter are shown in Fig. 21. By setting the dead time of the active rectifier σ_d=300ns and the phase difference φ_1=φ_2=5°, v_{gs_s1} and v_{gs_p1} always begin to turn to the high level after v_{ds_s1} and v_{ds_p1} are completely decreased to zero, which indicates that the ZVS operations are achieved in rectifiers and inverter.

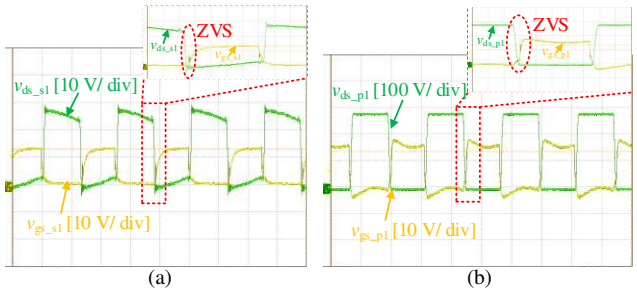

Fig. 21. Experimental waveforms of (a) v_{ds_s1} and v_{gs_s1}, (b) v_{ds_p1} and v_{gs_p1} when M_1=0.5·M_2 and I_{out}=30A.

C. Efficiency Comparison and Analysis

TABLE IV
SYSTEM SPECIFICATION AND PARAMETER VALUES OF THE SINGLE RECEIVER WPT SYSTEM

Symbol	*Value*	*Symbol*	*Value*	*Symbol*	*Value*
V_{dc}	350V	V_{out}	24V	I_{out}	10~50A
L_{sq}	14.4uH	C_{sq}	53.8nF	R_{sq}	60.1mΩ
L_{tq}	2.64uH	C_{tq}	239.9nF	R_{tq}	2.5mΩ
f	200kHz	S_1-S_4	IXFX420N10T	Air gap	30mm

Moreover, to offer a fair and complete comparison, a single receiver WPT system with the LCC-LCC topology is also built. Here, the transmitter is remained, while only the receiver coil and its compensation network are replaced in the single-rectifier receiver. The key parameters of the single receiver system are listed in TABLE IV, where L_{sq} is the receiver coil, while C_{sq}, L_{tq} and C_{tq} are the compensation elements in the LCC network. R_{sq} and R_{tq} are the ESRs in the corresponding loops. The coils of the magnetic coupler in the experimental setup are shown in Fig. 22(a).

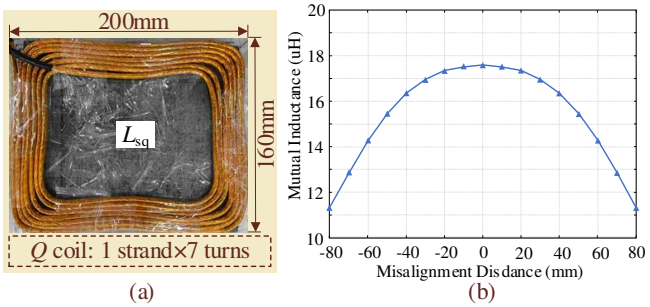

Fig. 22. (a)Structure and dimensions of the single receiver coil, (b) the mutual inductance M_q against the misalignment distance.

To achieve the same maximum system output current, the mutual inductance between the single receiver coil and the transmitter coil M_q is designed at 17.4uH when the magnetic coupler is well-aligned. The receiver coil is designed with 1-strand and 7-turns Litz-wire and the same size as the BP receiver coils. The mutual inductance against the misalignment distance is plotted in Fig. 22(b).

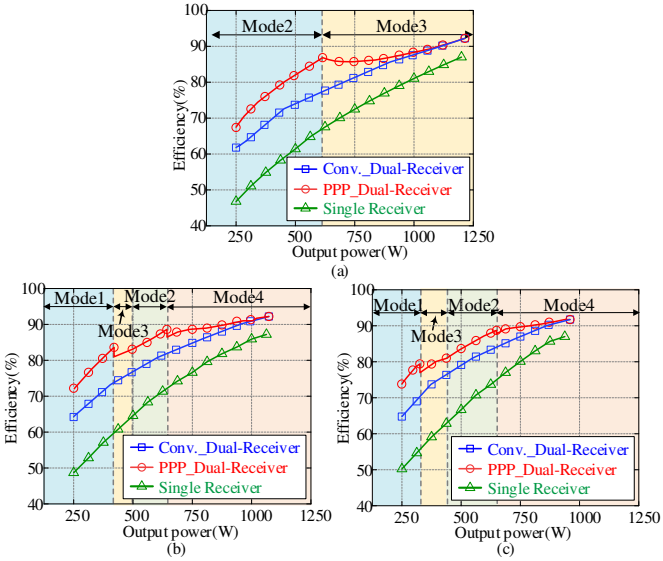

Fig. 23. The system efficiency against the output power when the misalignment distance (a) x=0mm, (b) x=-45mm, and (c) x=-60mm.

The trends of the overall system efficiency against the system output power with different misalignment distances are plotted in Fig. 23. When the magnetic coupler is well-aligned, the rectifiers operate under Mode 2 and Mode 3 at the corresponding load power demands with the proposed PPP control method, as shown in Fig. 23(a). Compared with the conventional power distribution method with the dual-receiver WPT system, the proposed method can improve the system efficiency by up to ~9%. When the mutual inductances are unbalanced, the receiver will operate respectively under four modes at the corresponding load power demands with the PPP method. In this situation, the proposed method can increase the system efficiency by ~10%, compared with the conventional method, as shown in Fig. 23(b) and (c). Meanwhile, the efficiency of the dual-receiver WPT system is always much higher than that of the single receiver WPT system with the whole operation range.

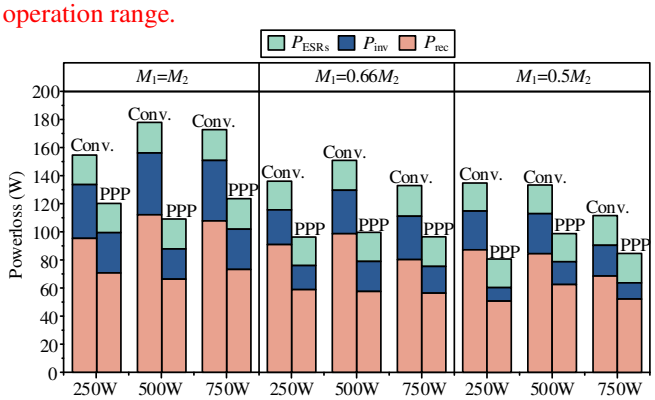

Fig. 24. The power loss distributions under different ratios of M_1 to M_2.

In Fig. 24, the power losses of each stage are analyzed under different mutual inductance conditions. Compared with the conventional power distribution method, when M_1=M_2, the proposed PPP control method can decrease the rectifier loss by ~26% @ P_{out}=250W, ~41% @ P_{out}=500W and ~31% @ P_{out}=750W. When M_1=0.66·M_2, the rectifier loss can be reduced by ~42% @ P_{out}=250W, ~26% @ P_{out}=500W and ~24% @ P_{out}=750W. Furthermore, the rectifier loss is reduced by ~45% @ P_{out}=250W, ~26% @ P_{out}=500W and by ~24% @ P_{out}=750W as M_1=0.5·M_2. Besides, the inverter loss is also reduced with the proposed PPP control method, while the ESRs are maintained at a low level. In conclusion, with the PPP control method, the rectifier loss is reduced apparently in the experimental setup, which indicates the effectiveness for efficiency improvement of the proposed method.

D. Dynamic Response

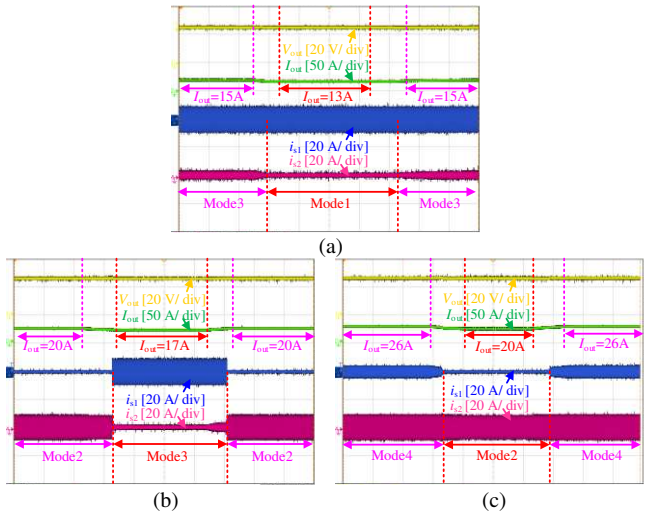

Fig. 25. Experimental dynamic response waveforms of V_{out}, I_{out}, i_{s1}, i_{s2} while (a) switching between Mode 1 and Mode 3, (b) switching between Mode 3 and Mode 2, and (c) switching between Mode 2 and Mode 4.

To verify the actual effect of the designed hysteresis control and PI control, the dynamic response waveforms of V_{out}, I_{out}, i_{s1} and i_{s2} when the load current is changing are provided in Fig. 25. With M_1=0.5M_2, when I_{out} varies slowly between 13A and 15A, the receiver is switched between Mode 1 and Mode 3. During the load variation process in Fig. 25(a), V_{out} can be maintained at a constant value without obvious oscillation or fluctuation, and no frequent switching phenomenon is observed. The same conclusion can also be obtained from Fig. 25(b), (c), which show the dynamic response waveforms when I_{out} varies between 17A (Mode 3) and 20A (Mode 2), and between 20A (Mode 2) and 26A (Mode 4). Thus, the dynamic performance of the control system can be well proved.

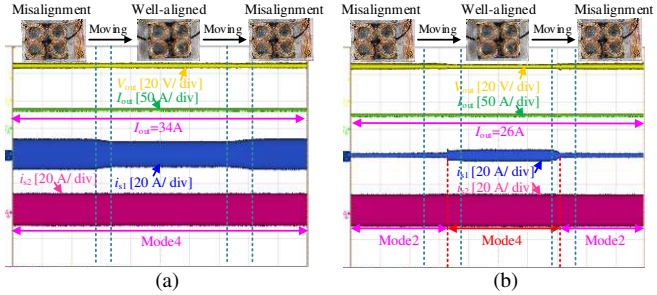

Fig. 26. Experimental dynamic response waveforms of V_{out}, I_{out}, i_{s1}, i_{s2} while the receiver is moving with (a) I_{out}=34A and (b) I_{out}=26A.

Moreover, for the dynamic applications, the waveforms when the receiver moves with a low speed are shown in Fig. 26.

While the receiver is moving, as shown in Fig. 26(a), V_{out} and I_{out} can be kept as 24V and 34A, and the receiver operates in Mode 4 stably. When I_{out} is set to 26A, the designed hysteresis control will switch the receiver into the corresponding operating mode with different misalignment conditions, as shown in Fig. 26(b). With the cooperation of the PI control and the hysteresis control, V_{out} and I_{out} can be maintained without noticeable overshoot or oscillation in the moving process, which indicates its good performance of dynamic response and stability.

E. Comparison with the Other Low-voltage and high-current output WPT system for LEVs charging

In the last decades, several methods have been investigated for the low-voltage and high-current power supply system, e.g., LEVs charging application to achieve a high power transfer efficiency [13], [14], [18], [19]. In [13], the dual-receiver-system with a DC-DC converter is adopted, which results in a low overall system efficiency. Besides, the volume of the receiver is also sacrificed due to the utilization of additional DC-DC converter. In [14], the series-series (S-S) compensation network is used in the 24V-75A output WPT system with ~89.9% efficiency. However, the multi-strands-paralleled Litz-wire in the receiver coil increases the cost and the weight of the magnetic coupler. In [18], the LCC-LCC compensation network is employed in the low-voltage and high-current output WPT system with the optimized current stress of the receiver coil. However, with only one receiver, the power loss in the receiver cannot be further reduced. In [19], with the S-S topology and the dual half-wave rectifier, multiple loads can be supplied with a 10A output current. Nevertheless, the receiver coil suffers from a large current stress due to its single receiver coil structure, which will lower the overall efficiency.

Compared with the above literatures, the main contribution of this paper is to reduce the ESRs loss and optimize the switching loss in the dual-receiver WPT system by reallocating the power flow through the receivers. When the load required current is varying with different misalignment conditions, the proposed system can obtain a stable output with a high overall efficiency. The comparisons are summarized and listed in TABLE V.

V. Conclusion

In this work, an efficiency improving method based on the PPP control is proposed for the dual-receiver WPT system. According to the mathematical analysis of the switching loss on the active rectifiers, the operation modes of the receiver are divided into four categories, and the corresponding characteristics for four modes are summarized. To reduce the rectifier switching loss and improve the overall system efficiency, a closed-loop control strategy is designed for selecting the operation mode of the rectifiers and regulating their conducting angles. To verify the proposed method, a 24V-50A prototype is set up. The experimental results show that, compared with the conventional power distribution method based on the impedance matching, the proposed PPP method can improve the efficiency by 6~7% with different misalignment situations, achieving as high as over 92.2% at the heavy load conditions.

TABLE V
Summary and Comparison of the Previous Low-Voltage and High-Current WPT Systems

Reference	Power regulating method	Circuit structure	Compensation network	Output characteristic	Receiver coil size	Operating frequency	Coupling coefficient	Output power	Efficiency
[13]	DC-DC converter	Dual receiver	S-P	30V-10A	300mm*300mm*26mm	10kHz	0.35	300W	88%
[14]		Singe receiver	S-S	24V-75A	220mm*220mm*10mm	85kHz	0.7	1.8kW	89.9%
[18]		Singe receiver	LCC-LCC	24V-75A	220mm*220mm*10mm	85kHz	0.68~0.92	1.8kW	88%
[19]	Half wave rectifier	Singe receiver	S-S	48V-10A		85kHz	0.23	480W	90.93%
This paper	Active Rectifier	Dual receiver	LCC-LCC	24V-50A	200mm*160mm*25mm	200kHz	0.35	1.2kW	92.2%

References

[1] M. Fu, C. Ma, and X. Zhu, "A cascaded boost–buck converter for high-efficiency wireless power transfer systems," in *IEEE Trans. on Ind. Informat.*, vol. 10, no. 3, pp. 1972-1980, Aug. 2014.

[2] J. Feng, Q. Li, F. Lee, and M. Fu, "Transmitter coils design for free-positioning omnidirectional wireless power transfer system," in *IEEE Trans. on Ind. Informat.*, vol. 15, no. 8, pp. 4656-4664, Aug. 2019.

[3] J. Zhu, Y. Ban, Y. Zhang, Z. Yan, R. Xu, and C. Mi, "Three-coil wireless charging system for metal-cover smartphone applications," in *IEEE Trans. on Power Electron.*, vol. 35, no. 5, pp. 4847-4858, May. 2020.

[4] M. Huang, Y. Lu, and R. Martins, "A reconfigurable bidirectional wireless power transceiver for battery-to-battery wireless charging," in *IEEE Trans. on Power Electron.*, vol. 34, no. 8, pp. 7745-7753, Aug. 2019.

[5] Y. Li, J. Hu, X. Li, F. Chen, Q. Xu, R. Mai, and Z. He, "Analysis, design, and experimental verification of a mixed high-order compensations-based WPT system with constant current outputs for driving multi-string LEDs," in *IEEE Trans. on Ind. Electron.*, vol. 67, no. 1, pp. 203-213, Jan. 2020.

[6] Z. Yan, Q. Siyao, Q. Zhu, L. Huang, and A. Hu, "A simple brightness and color control method for LED lighting based on wireless power transfer," in *IEEE Access*, vol. 6, pp. 51477-51483, Sept. 2018.

[7] D. Patil, M. McDonough, J. Miller, B. Fahimi, and P. Balsara, "Wireless power transfer for vehicular applications: overview and challenges," in *IEEE Trans. on Transp. Electrific.*, vol. 4, no. 1, pp. 3-37, Mar. 2018.

[8] A. Mohamed, A. Berzoy, and O. Mohammed, "Experimental Validation of comprehensive steady-state analytical model of bidirectional WPT system in EVs applications," in *IEEE Trans. on Veh. Technol.*, vol. 66, no. 7, pp. 5584-5594, Jul. 2017.

[9] L. Zhao, D. Thrimawithana, and U. Madawala, "Hybrid bidirectional wireless EV charging system tolerant to pad misalignment," in *IEEE Trans. on Ind. Electron.*, vol. 64, no. 9, pp. 7079-7086, Sept. 2017.

[10] A. Babaki, S. Vaez-Zadeh, A. Zakerian, and G. Covic, "Variable-frequency retuned WPT system for power transfer and efficiency improvement in dynamic EV charging with fixed voltage characteristic," in *IEEE Trans. on Energy Convers.*, Early Access, doi: 10.1109/TEC.2020.3048196.

[11] W. Zhang, J. White, A. Abraham, and C. Mi, "Loosely coupled transformer structure and interoperability study for EV wireless charging systems," in *IEEE Trans. on Power Electron.*, vol. 30, no. 11, pp. 6356-6367, Nov. 2015.

[12] Y. Li, J. Hu, T. Lin, X. Li, F. Chen, Z. He, and R. Mai, "A new coil structure and its optimization design with constant output voltage and constant output current for electric vehicle dynamic wireless charging," in *IEEE Trans. on Ind. Informat.*, vol. 15, no. 9, pp. 5244-5256, Sept. 2019.

[13] A. Zaheer, G. Covic, and D. Kacprzak, "A bipolar pad in a 10-kHz 300-W distributed IPT system for AGV applications," in *IEEE Trans. on Ind. Electron.*, vol. 61, no. 7, pp. 3288-3301, Jul. 2014.

[14] F. Lu, Y. Zhang, H, Zhang, C. Zhu, L, Diao, M. Gong, W. Zhang, and C. Mi, "A low-voltage and high-current inductive power transfer system with low harmonics for automatic guided vehicles," in *IEEE Trans. on Veh. Technol.*, vol. 68, no. 4, pp. 3351-3360, Apr. 2019.

[15] Z. Zhang and B. Zhang, "Omnidirectional and efficient wireless power transfer system for logistic robots," in *IEEE Access*, vol. 8, pp. 13683-13693, Jan. 2020.

[16] X. Dai, J. Wu, J. Jiang, R. Gao, and U. Madawala, "An energy injection method to improve power transfer capability of bidirectional WPT system with multiple pickups," in *IEEE Trans. on Power Electron.*, vol. 36, no. 5, pp. 5095-5107, May. 2021.

[17] H. He, S. Wang, Y. Liu, C. Jiang, X. Wu, B. Wei, and B. Jiang, "Maximum efficiency tracking for dynamic WPT system based on optimal input voltage matching," in *IEEE Access*, vol. 8, pp. 215224-215234, Dec. 2020.

[18] F. Lu, H. Zhang, C. Zhu, L, Diao, M. Gong, W. Zhang, and C. Mi, "A tightly coupled inductive power transfer system for low-voltage and high-current charging of automatic guided vehicles," in *IEEE Transactions on Ind. Electron.*, vol. 66, no. 9, pp. 6867-6875, Sept. 2019.

[19] C. Zhu, J. Yu, Y. Gu, J. Gao, H. Yang, R. Mai, Y. Li, and Z. He, "Analysis and design of cost-effective WPT Systems with dual independently regulatable outputs for automatic guided vehicles," in *IEEE Trans. on Power Electron.*, vol. 36, no. 6, pp. 6183-6187, Jun. 2021.

[20] Y. Li, T. Lin, R. Mai, L. Huang, and Z. He, "Compact double-sided decoupled coils-based WPT systems for high-power applications: analysis, design, and experimental verification," in *IEEE Trans. on Transp. Electrific.*, vol. 4, no. 1, pp. 64-75, Mar. 2018.

[21] S. Zhou and C. Mi, "Multi-paralleled LCC reactive power compensation networks and their tuning method for electric vehicle dynamic wireless charging," in *IEEE Trans. on Ind. Electron.*, vol. 63, no. 10, pp. 6546-6556, Oct. 2016.

[22] U. Schwalbe, M. Schilling, B. Koehnlechner, and T. Reimann, "Challenges in low-voltage high-current applications - Fathom the limits in system design," in *Proc. Int. Conf. Integr. Power Electron.*, 2016, pp. 1–7.

[23] B. Zhao, Q. Song, W. Liu, and Y. Sun, "Overview of dual-active-bridge isolated bidirectional DC-DC converter for high-frequency-link power-conversion system," in *IEEE Trans. on Power Electron.*, vol. 29, no. 8, pp. 4091-4106, Aug. 2014.

[24] S. Inoue and H. Akagi, "A bidirectional isolated DC-DC converter as a core circuit of the next-generation medium-voltage power conversion system," in *IEEE Trans. on Power Electron.*, vol. 22, no. 2, pp. 535-542, Mar. 2007.

[25] Z. Yan, B. Yang, H. Liu, C. Chen, M. Waqas, R. Mai, and Z. He, "Efficiency improvement of wireless power transfer based on multi-transmitter system," in *IEEE Trans. on Power Electron.*, vol. 35, no. 9, pp. 9011-9023, Sept. 2020.

[26] G. Ning, S. Wang, G. Zheng, Y. Liu, and M. Fu, "A novel passive current sharing method for a two-transmitter one-receiver WPT system," *2020 IEEE 9th International Power Electronics and Motion Control Conference (IPEMC2020-ECCE Asia)*, 2020, pp. 985-990.

[27] M. Fu, H. Yin, M. Liu, Y. Wang, and C. Ma, "A 6.78 MHz multiple-receiver wireless power transfer system with constant output voltage and optimum efficiency," in *IEEE Trans. on Power Electron.*, vol. 33, no. 6, pp. 5330-5340, Jun. 2018.

[28] M. Fu, T. Zhang, C. Ma, and X. Zhu, "Efficiency and optimal loads analysis for multiple-receiver wireless power transfer systems," in *IEEE Trans. on Microw. Theory Tech.*, vol. 63, no. 3, pp. 801-812, Mar. 2015.

[29] D. Pehrman, Y. Liu, C. Cui, and X. Huang, "Loss reduction by synchronous rectification in a 50 kW SiC-based inductive power transfer system," *IECON 2020 The 46th Annual Conference of the IEEE Industrial Electronics Society*, 2020, pp. 3907-3912.

[30] R. Bosshard and J. Kolar, "All-SiC 9.5 kW/dm^3 on-board power electronics for 50 kW/85 kHz automotive IPT system," in *IEEE J.Emerg. Sel. Topics Power Electron.*, vol. 5, no. 1, pp. 419-431, Mar. 2017.

[31] A. Q. Cai and L. Siek, "A 2-kW, 95% efficiency inductive power transfer system using gallium nitride gate injection transistors," in *IEEE J.Emerg. Sel. Topics Power Electron.*, vol. 5, no. 1, pp. 458-468, Mar. 2017.

[32] T. Mishima and E. Morita, "High-frequency bridgeless rectifier based ZVS multi-resonant converter for inductive power transfer featuring high-voltage GaN-HFET," in *IEEE Trans. on Ind. Electron.*, vol. 64, no. 11, pp. 9155-9164, Nov. 2017.

[33] T. Mishima and E. Morita, "Comparative evaluation of secondary-side ZVS-PWM controlled GaN-HFET resonant converters for inductive power transfer," *2017 IEEE Energy Conversion Congress and Exposition (ECCE)*, 2017, pp. 2610-2617.

[34] Y. Li, S. Liu, X. Zhu, J. Hu, M. Zhang, R. Mai, and Z. He, "Extension of ZVS region of series–series WPT Systems by an auxiliary variable inductor for improving efficiency," in *IEEE Trans. on Power Electron.*, vol. 36, no. 7, pp. 7513-7525, Jul. 2021.

[35] Y. Jiang, L. Wang, J. Fang, R. Li, R. Han, and Y. Wang, "A high-efficiency ZVS wireless power transfer system for electric vehicle charging with variable angle phase shift control," in *IEEE J.Emerg. Sel. Topics Power Electron.*, vol. 9, no. 2, pp. 2356-2372, Apr. 2021.

[36] Y. Jiang, L. Wang, J. Fang, C. Zhao, K. Wang, and Y. Wang, "A joint control with variable ZVS angles for dynamic efficiency optimization in wireless power transfer system," in *IEEE Trans. on Power Electron.*, vol. 35, no. 10, pp. 11064-11081, Oct. 2020.

[37] D. Christen and J. Biela, "Analytical switching loss modeling based on datasheet parameters for MOSFETs in a half-bridge," in *IEEE Trans. on Power Electron.*, vol. 34, no. 4, pp. 3700-3710, Apr. 2019.

[38] D. Neumayr, M. Vöhringer, N. Chrysogelos, G. Deboy, and J. Kolar, "P^{3}DCT—partial-power pre-regulated DC transformer," in *IEEE Trans. on Power Electron.*, vol. 34, no. 7, pp. 6036-6047, Jul. 2019.

[39] J. Zientarski, M. Martins, J. Pinheiro, and H. Hey, "Evaluation of power processing in series-connected partial-power converters," in *IEEE J.Emerg. Sel. Topics Power Electron.*, vol. 7, no. 1, pp. 343-352, March 2019.

[40] V. Iyer, S. Gulur, G. Gohil, and S. Bhattacharya, "An approach towards extreme fast charging station power delivery for electric vehicles with partial power processing," in *IEEE Trans. on Ind. Electron.*, vol. 67, no. 10, pp. 8076-8087, Oct. 2020.

[41] J. Anzola, I. Aizpuru, A. Arruti, A. Alacano, and C. Bernal, "Review of architectures based on partial power processing for DC-DC applications," in *IEEE Access*, vol. 8, pp. 103405-103418, Jun. 2020.

[42] N. Bac, D. Vilathgamuwa, and U. Madawala, "A SiC-based matrix-converter topology for inductive power transfer system," in *IEEE Trans. on Power Electron.*, vol. 29, no. 8, pp. 4029-4038, Aug. 2014.

[43] H. Raee, A. Rabiei, and T. Thirnger, "Analytical prediction of switching losses in MOSFETs for variable drain-source voltage and current applications," *2013 IEEE 8th Conference on Industrial Electronics and Applications (ICIEA)*, 2013, pp. 705-709.

[44] W. Eberle, Z. Zhang, Y. Liu and P. Sen, "A practical switching loss model for buck voltage regulators," in *IEEE Trans. on Power Electron.*, vol. 24, no. 3, pp. 700-713, Mar. 2009.

[45] F. Lu, H. Zhang, H. Hofmann, W. Su, and C. Mi, "A dual-coupled LCC compensated IPT system with a compact magnetic coupler," *IEEE Trans. Power Electron.*, vol. 33, no. 7, pp. 6391–6402, Jul. 2018.

[46] H. Zhang, C. Zhu and F. Lu, "A compact and low-distortion inductive charging system for automatic guided vehicles based on LCC compensation and integrated magnetic coupler," *2019 IEEE Transportation Electrification Conference and Expo (ITEC)*, 2019, pp. 1-5.

[47] P. Zhang, M. Saeedifard, O. Onar, Q. Yang and C. Cai, "A field enhancement integration design featuring misalignment tolerance for wireless EV charging using LCL topology," in *IEEE Trans. on Power Electron.*, vol. 36, no. 4, pp. 3852-3867, April 2021.

Response: Efficiency Improvement of Dual-Receiver WPT Systems Based on Partial Power Processing Control

Dear Editor and Reviewers,

The authors would like to thank all the reviewers for their encouraging and insightful comments. The manuscript has been revised, considering all the comments from the reviewers and editor. We have addressed the comments with all necessary modifications and responses. The salient additions to the paper were highlighted **in red**. In addition, the detailed clarifications to respective reviewers are listed as follows.

■ Associate Editor

Comments to the Author:

Four reviewers found the paper useful but pointed out deficiencies that should be addressed. Revision is recommended to improve the paper according to the comments of the reviewers.

Response: Thanks a lot for your reminding us of addressing comments. We have considered all the reviewers' comments seriously and carefully. We hope our detailed explanations and new works will satisfy the reviewers.

■ **Reviewer: #1**

Comments to the Author:

(1) The paper focuses on wireless charging for light electric vehicles, like AGV. In this scenario, a small size, lightweight, simple receiver is desired. The proposed dual-receiver IPT and the LCC-LCC topology seem not suitable for the proposed application. The simple SS is more attractive.

Response: Thanks for your valuable review. Exactly, the simple SS compensation network or LLC compensation with only one receiver will cost less passive and active elements. However, considering the power transfer capacity, the power loss and the misalignment tolerance, adopting the dual receiver WPT system with the LCC-LCC compensation networks is more reasonable and adaptive. Although more elements are employed in the LCC-LCC compensation networks, these passive elements could even be integrated into the coupler, while the size and weight of the receiver are not increased apparently [R1]-[R3]. Here, the detailed analysis is provided as follow.

1) Power transfer capacity

In the past researches of the low-voltage and high-current output WPT systems, the single receiver topology with one receiver coil and one rectifier is already reported [R4]-[R5]. **However, to increase the power transfer capacity and release the current stress of the low-voltage and high-current WPT system, the dual receiver topology with two receiver coils and two rectifiers is also attractive**. Due to the ampacity limitation of the Litz-wire, the MOSFETs in the active rectifier and other passive elements, increasing the number of the power transfer channels is an effective way to reduce the equivalent series resistances (ESRs) loss and the conducting loss of the rectifier. Since the currents in each power transfer channel can be halved, the total ESRs loss and rectifier conducting loss can also be halved, which could obviously improve the system power transfer capacity.

2) Power loss

While adopting the dual receiver system to increase the power transfer capacity and reduce the power loss on the receiver side, the compensation network should also be well selected and designed. To provide a flat electromagnetic field and a constant current output characteristic, the LCC-LCC compensation network is adopted. Compared to the conventional SS compensation network, **the LCC-LCC network not only well limits the transmitter coil current while misalignment occurs, but also provide more freedom degrees to release the coil current, which further reduces the ESRs loss and the ampacity requirements of the receiver coils [R5]**. By designing the parameters of the LCC networks, the current stress of the receiver coils can be further reduced. In the revised manuscript, a 24V-50A output WPT

system is rebuilt, and the key parameters are listed in TABLE RI. When the system output current is up to 50A, the currents in the receiver coils with different compensation networks are listed in TABLE RII. In the rebuilt experimental setup, due to the characteristic of the LCC-LCC compensation networks, the current in each receiver coil is lower than 7A, which is much lower than that of the SS compensation with the single receiver and dual-receivers. Moreover, the ESRs loss on the compensation inductors is also limited because of its low ESRs value.

TABLE RI

SYSTEM SPECIFICATION AND PARAMETER VALUES OF THE REBUILT EXPERIMENTAL SETUP

Symb.	*Val.*	*Symb.*	*Val.*	*Symb.*	*Val.*
V_{dc}	350V	V_{out}	24V	I_{out}	5~50A
L_r	29.5uH	C_r	21.46nF	R_r	40mΩ
L_p	90.4uH	C_p	10.4nF	R_p	220.1mΩ
L_{t1}	2.63uH	C_{t1}	240.8nF	R_{t1}	2.9mΩ
L_{t2}	2.64uH	C_{t2}	239.9nF	R_{t2}	2.9mΩ
L_{s1}	6.92uH	C_{s1}	147.6nF	R_{s1}	23.0mΩ
L_{s2}	7.09uH	C_{s2}	142.3nF	R_{s2}	24.1mΩ
f	200kHz	S_1-S_8	IXFX420N10T	A_{rec}+ B_{rec}	138ns
Air gap	30mm	P_1-P_4	C3M0021120D	A_{inv}+ B_{inv}	34.2ns

TABLE RII

COMPARISON OF THE RECEIVER COIL CURRENTS WITH DIFFERENT RECEIVER TOPOLOGIES

SS compensation with a single receiver	*SS compensation with dual-receiver*	*LCC-LCC compensation with dual-receiver*
50A	25A	7A

Meanwhile, the LCC circuit can reduce the harmonic currents, especially in short gap applications, while the harmonic currents in the SS compensation system will effectively induce extra power losses [R5]. Besides, here is another issue while adopting the SS compensation networks in the dual receiver WPT system. Since the circuit characteristic of the SS compensation network, while the mutual inductance between the transmitter coil and the two receiver coils are not balanced, the circulation phenomenon will occur, which seriously affects the overall system efficiency. However, in the dual receiver WPT system with LCC-LCC compensation networks, the ratio of receiver output currents is only determined by the mutual inductance M_1 and M_2 ratio, and no circular current will be produced on the receiver side. In conclusion, adopting the LCC-LCC compensation network in this situation is an available way to improve the ESRs loss and avoid the extra loss caused by harmonic currents and circulation.

3) Misalignment tolerance

Compared with the single large coil, the BP coil structure used in this paper is widely introduced in much literature before. **With two individual coils are placed at both ends of the receiver, the magnetic field at the BP coil structure-based receiver side will be more uniform, and a better misalignment**

tolerance can be achieved [R6]-[R9].

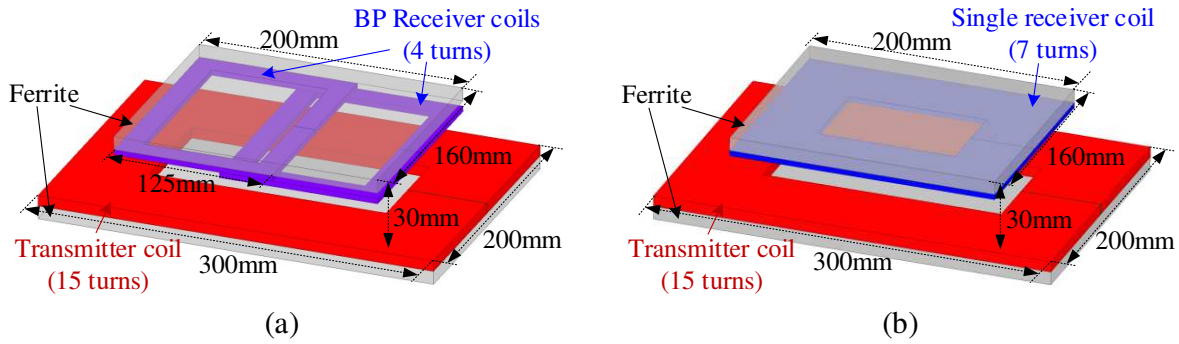

Fig. R1. The model and dimensions of the magnetic couplers (a) with the BP receiver coils and (b) the single Q receiver coil.

To quantize the improvement of the misalignment tolerance, the simulation models of these two couplers are built in ANSYS MAXWELL software. The model and dimensions of the magnetic couplers are shown in Fig. R1. Here, in the revised manuscript, a new coupler size is adopted. The length and width of the transmitter coil are still 300mm and 200mm, while the length and width of the receiver coil are reduced to 200mm and 160mm for suiting the actual Light Electric Vehicles (LEVs). The trends of the simulated mutual inductances against the misalignment tolerance are plotted in Fig. R2. With the same size of the magnetic coupler and the same maximum mutual inductance, **compared with that of the BP structure, the mutual inductance of the single receiver coil decreases more when the misalignment occurs**, which well prove the improvement of the misalignment tolerance with the BP receiver coils.

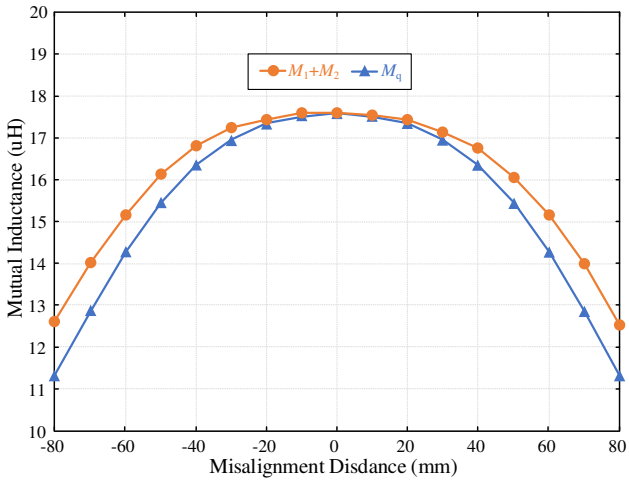

Fig. R2. The simulated mutual inductance between the transmitter coil and the receiver coils against the misalignment distance.

4) Size and weight

Although adopting two receivers seems to increase the complexity of the WPT system, the size and weight can be limited. As shown in Fig. R1, with the same coupler size and fully covered ferrite, the costs of the ferrite are totally the same in the single large coil and the BP coils. Meanwhile, the 20mm^2-Litz-wire is used in this design. The single large coil costs ~4.83m two strands in parallel Litz-wire. Besides, the BP receiver coils totally cost just ~4.24m single strand Litz-wire in total with half current

stress.

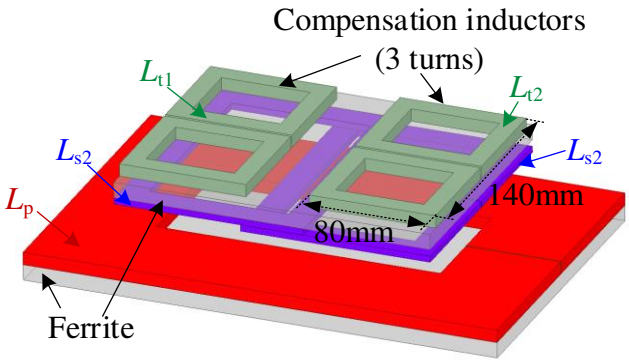

Fig. R3. The model and dimensions of the compensation inductors integrated into the magnetic coupler.

To make the system more compact, the compensation inductors can also be integrated into the magnetic coupler. Similar ideas are already proposed in [R1]-[R3]. As shown in Fig. R3, **by placing DD coils at the outside of the ferrite in the receiver as the inductors, the size and weight of the compensation inductors can be saved without any extra ferrite.** The trends of simulated mutual inductances between each coil integrated into the coupler are plotted in Fig. R4. Here, M_1 and M_2 are the mutual inductances between the transmitter coil and the individual BP receiver coil. $M_{p\text{-}t1}$ and $M_{p\text{-}t2}$ are the mutual inductances between the transmitter coil and the DD compensation inductors. $M_{s1\text{-}t1}$, $M_{s1\text{-}t2}$, $M_{s2\text{-}t1}$ and $M_{s2\text{-}t2}$ indicate the mutual inductances between the BP receiver coils and the DD compensation inductors. In addition, $M_{s1\text{-}s2}$ indicates the cross-coupling between the BP receiver coils, while $M_{t1\text{-}t2}$ indicates the cross-coupling between the DD compensation inductors. The simulation results show that, **with the BP receiver coil structure and the integrated DD inductors, all the coils at the receiver side can be well decoupled, and the compensation inductors are well decoupled with the transmitter coil. Then, the load-independent constant output current can be achieved.**

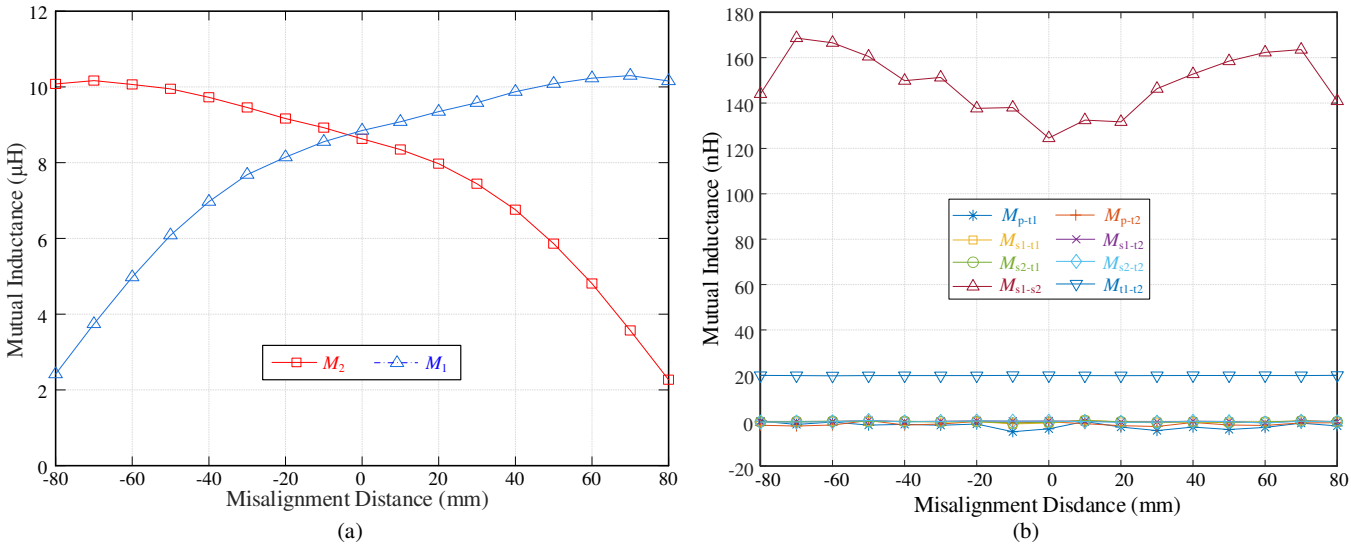

Fig. R4. The simulated mutual inductance between each coil in the coupler against the misalignment distance.

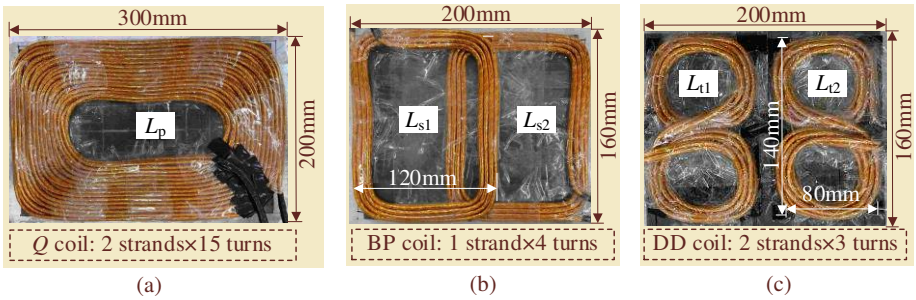

Fig. R5. Structure and dimensions of (a) the transmitter coil, (b) the BP receiver coils and (c) the DD comparison inductors.

The experimental setup of the coils in the designed WPT system is shown in Fig. R5, since the compensation inductors are integrated with the receiver coils. The extra ferrite for these inductors is not ever required. Meanwhile, the cost of the Litz-wire for the inductors is also limited, which is only 2.88m two strands in parallel Litz-wire in this paper. Thus, **the size and weight of the proposed receiver can be well limited.**

The new experimental setup is shown in Fig. R6. Benefits of the high-frequency characteristic of the capacitors, while the system frequency is increased, the ESRs of the capacitors are reduced, which means that fewer capacitors are required in the setup for the high current conditions. In addition, to further reduce the size of the passive elements, the compensated capacitors in one LCC compensation network C_{s1}, C_{t1} and C_{s2}, C_{t2} can also be integrated as entire capacitor elements since they share a common node, as shown in Fig. R6.

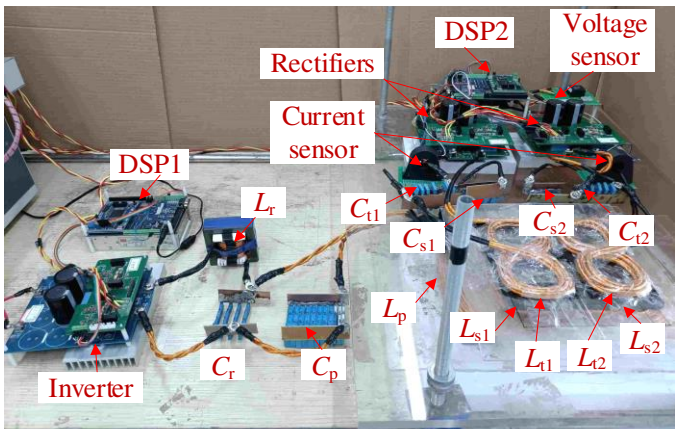

Fig. R6. Experimental setup in the revised manuscript.

In conclusion, the comparison between the simple SS compensated system and the LCC-LCC compensated dual-receiver system is listed in TABLE RIII. **The LCC-LCC compensated dual-receiver system has advantages in power transfer capacity, power loss and misalignment tolerance. Meanwhile, though more passive elements are required in the proposed WPT system, the increase of the size and weight of the receiver can be well limited by some integration methods.**

TABLE RIII

COMPARISON OF THE RECEIVER COIL CURRENTS WITH DIFFERENT COMPENSATION NETWORKS

	Simple SS compensated system	*LCC-LCC compensated dual-receiver system*
Power transfer capacity	Low	High
Power loss	High	Low
Misalignment tolerance	Ordinary	Improved
Size and weight	Small and light	Well limited

[R1] F. Lu, H. Zhang, H. Hofmann, W. Su, and C. Mi, "A dual-coupled LCC compensated IPT system with a compact magnetic coupler," *IEEE Trans. Power Electron.*, vol. 33, no. 7, pp. 6391–6402, Jul. 2018.

[R2] H. Zhang, C. Zhu and F. Lu, "A Compact and Low-Distortion Inductive Charging System for Automatic Guided Vehicles Based on LCC Compensation and Integrated Magnetic Coupler," *2019 IEEE Transportation Electrification Conference and Expo (ITEC)*, 2019, pp. 1-5.

[R3] P. Zhang, M. Saeedifard, O. C. Onar, Q. Yang and C. Cai, "A Field Enhancement Integration Design Featuring Misalignment Tolerance for Wireless EV Charging Using LCL Topology," in *IEEE Trans. on Power Electron.*, vol. 36, no. 4, pp. 3852-3867, April 2021.

[R4] F. Lu, Y. Zhang, H, Zhang, C. Zhu, L, Diao, M. Gong, W. Zhang, and C. Mi, "A low-voltage and high-current inductive power transfer system with low harmonics for automatic guided vehicles," in *IEEE Trans. on Veh. Technol.*, vol. 68, no. 4, pp. 3351-3360, Apr. 2019.

[R5] F. Lu, H. Zhang, C. Zhu, L, Diao, M. Gong, W. Zhang, and C. Mi, "A tightly coupled inductive power transfer system for low-voltage and high-current charging of automatic guided vehicles," in *IEEE Trans. on Ind. Electron.*, vol. 66, no. 9, pp. 6867-6875, Sept. 2019.

[R6] G. Covic, M. Kissin, D. Kacprzak, N. Clausen, and H. Hao, "A bipolar primary pad topology for EV stationary charging and highway power by inductive coupling," *Proc. IEEE Energy Convers. Congr. Expo.*, Phoenix, AZ, USA, 2011, pp. 1832–1838.

[R7] A. Zaheer, D. Kacprzak, and G. Covic, "A bipolar receiver pad in a lumped IPT system for electric vehicle charging applications," *Proc. IEEE Energy Convers. Congr. Expo.*, Raleigh, NC, USA, 2012, pp. 283–290.

[R8] A. Zaheer, G. Covic, and D. Kacprzak, "A bipolar pad in a 10-kHz 300-W distributed IPT system for AGV applications," in *IEEE Trans. Ind. Electron.*, vol. 61, no. 7, pp. 3288–3301, Jul. 2014.

[R9] F. Lin, S. Kim, G. Covic, and J. Boys, "Effective coupling factors for series and parallel tuned secondaries in IPT systems using bipolar primary pads," in *IEEE Trans. Transp. Electrif.*, vol. 3, no. 2, pp. 434–444, Jun. 2017.

(2) The author claimed that this work is for the low-voltage and high-current charging case. However, in the experiment, the voltage is 72V and the current is lower than 10A. It is not a real low-voltage and high-current application. The typical low voltage should be 24V/36V/48V and the high-current should be more than 50A. In this case, the equivalent resistance is very small and receiver coils design will be difficult, which is the main challenge.

Response: Thanks for your review and suggestion. According to your suggestions, **we rebuilt a 24V-50A output WPT system in the revised manuscript to verify the performance of the proposed PPP method. The LCC-LCC compensated dual-receiver topology is adopted**, as shown in Fig. R7.

The magnetic coupler and the rebuilt experimental setup are shown in Fig. R5 and Fig. R6. The

parameters of the rebuilt experimental setup are introduced in TABLE RI. As shown in Fig. R5(a), the transmitter coil is in the unipolar square shape. The transmitter coil current I_p is only about 9A, and the two-strand paralleled Litz-wire is adopted in the transmitter coil. Due to the well-designed LCC-LCC compensation parameters for the BP receiver coil, the maximum current in the receiver coils is limited at 7A, and single-strand Litz-wire is also adopted, as shown in Fig. R5(b). For the compensation inductors, since the RMS value of the current is approaching more than 27A, the two-strand Litz-wire is used to make L_{t1} and L_{t2}, as shown in Fig. R5(c). The power MOSFETs are also reselected. At the receiver side, the low-voltage-low-conducting-resistance MOSFET IXFX420N10T is selected for reducing the conducting loss of the active rectifier.

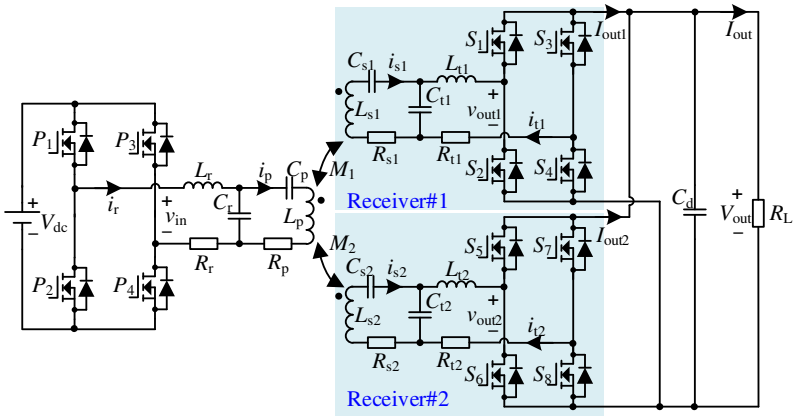

Fig. R7. Schematic diagram of the LCC-LCC compensated dual-receiver WPT system.

With the rebuilt experimental setup, while the magnetic coupler is well-aligned, the output current can be up to 50A, and the maximum power transfer efficiency can be obtained at 92.4%. According to the results of the rebuilt setup, we can find that the WPT system with the proposed PPP method performs higher system overall efficiency than the system with the conventional power distribution method, and the power loss of the rectifiers, mainly the switching loss, has been apparently reduced. A detailed analysis of the experimental results is introduced in the revised manuscript.

(3) The caption of Fig.1 is incorrect.

Response: Thanks for your careful review. We have corrected the caption as "Schematic diagram of the dual receiver WPT system with LCC-LCC compensation networks." in the revised manuscript, and the modification are highlighted **in red**.

(4) In the active rectifier, the duty cycle is not always 50%, why? For efficiency optimization? This will induce additional power loss and reduce the power. When the misalignment occurs, the duty cycle becomes smaller, which will further decrease the power in the misaligned case. This control is adverse to

the power output.

Response: Thanks for your careful review. We do increase the active rectifier's duty cycle to 50% when the system is fully loaded. However, when the load required power is reduced, the active rectifiers should be regulated to suit the load demands, and their duty cycle will be decreased. The main contribution of this paper is to improve the overall system efficiency by adjusting the power distribution in different power channels, while the active rectifiers are regulated for adapting different load and different misalignment conditions.

(5) In the conventional design, the currents are more balanced, which aims to achieve the minimum coil loss, which should be smaller than the PPP strategy. However, in fig.20, it seems the conventional method does not show the advantage in ESR loss.

Response: Thanks for your careful review. As you said, the ESRs loss in the receiver coils with the conventional power distribution method is lower than that of the PPP control. However, as we mentioned before, **since the current stress of the receiver coils is well limited by designing the parameters of the LCC-LCC compensation networks, the actual ESRs losses on the receiver coils occupy only a tiny part of the overall ESRs loss.** Meanwhile, the ESRs loss of the LC loop in the primary side, i.e., L_r and C_r, is also improved with the PPP control, which occupies a significant part of the overall ESRs loss. Thus, the advantage of the ESRs loss with the conventional power distribution method is not apparent.

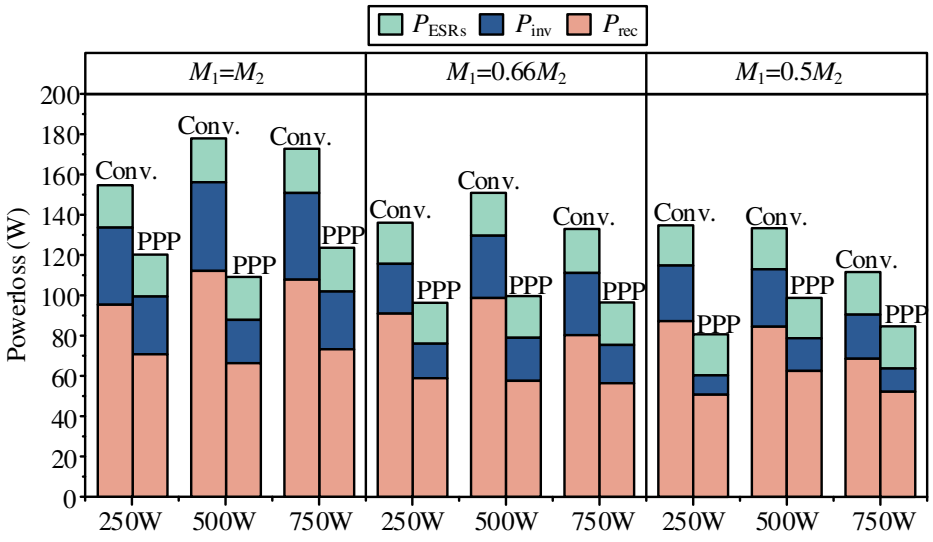

Fig. R8. The power losses division with different ratios between M_1 and M_2.

Here, with the rebuilt experimental setup, the ESRs loss of each part are listed in Fig. R8. According to the experimental results, we can obtain a similar conclusion that the system with the conventional power distribution method performs no apparent advantage in improving ESRs loss while the ESRs and the currents of the receiver coils are well limited.

(6) What are the transfer distance and the coefficients? Please provide such information in the experiment part.

Response: Thanks for your review. We apologize that the parameters of the transfer distance and the couple coefficients are not shown in the table of the experimental setup parameters. Here, to provide more persuasive experimental results, we rebuilt a 24V-50A output experimental setup, and the corresponding parameters are shown in TABLE RIV. The transfer distance, i.e., the air gap of the magnetic coupler, is 30mm. Meanwhile, the coupling coefficient between the transmitter coil and the single BP receiver coil is about 0.35 when the transmitter and the receiver are well-aligned.

TABLE RIV

SYSTEM SPECIFICATION AND PARAMETER VALUES

Symb.	*Val.*	*Symb.*	*Val.*	*Symb.*	*Val.*
V_{dc}	350V	V_{out}	24V	I_{out}	5~50A
L_r	29.5uH	C_r	21.46nF	R_r	40mΩ
L_p	90.4uH	C_p	10.4nF	R_p	220.1mΩ
L_{t1}	2.63uH	C_{t1}	240.8nF	R_{t1}	2.9mΩ
L_{t2}	2.64uH	C_{t2}	239.9nF	R_{t2}	2.9mΩ
L_{s1}	6.92uH	C_{s1}	147.6nF	R_{s1}	23.0mΩ
L_{s2}	7.09uH	C_{s2}	142.3nF	R_{s2}	24.1mΩ
f	200kHz	S_1-S_8	IXFX420N10T	A_{rec}+ B_{rec}	138ns
Air gap	30mm	P_1-P_4	C3M0021120D	A_{inv}+ B_{inv}	34.2ns

■ **Reviewer: #2**

Comments to the Author

(1) In general, dual receiver systems need to use DCDC to prevent circulation. However, DCDC has not been added to this system. Will circulation occur when M1 is not equal to M2? The key current waveform should be given to illustrate.

Response: Thanks for your careful review. Indeed, the circulation phenomenon easily occurs in the SS compensated dual-receiver WPT system while M_1 is not equal to M_2. **In this paper, the authors utilize the LCC-LCC compensation network, which suppresses the circulation by its characteristics. Therefore, the DC-DC converter is replaced with the active rectifier regulated by the VAPS control method.** The characteristic difference of the SS and LCC-LCC will be analyzed as follow:

1) For the SS compensation networks

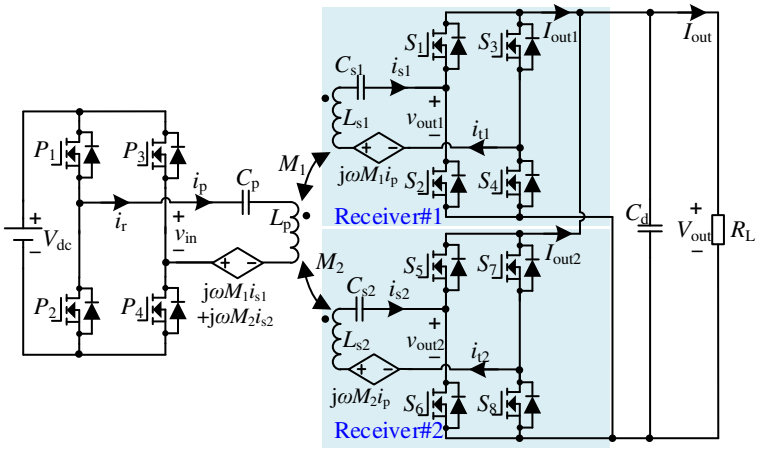

Fig. R9. The dual-receiver WPT system with SS compensation network.

When the SS compensated WPT system is resonant, the receiver coil currents can be expressed as

$$\begin{cases} \dot{I}_{s1} = \dfrac{\dot{V}_{in(1)}}{j\omega M_1} \\ \dot{I}_{s2} = \dfrac{\dot{V}_{in(1)}}{j\omega M_2} \end{cases}. \tag{R1}$$

The transmitter coil current i_p is related to the two receivers. Thus the current must satisfy

$$\dot{I}_p = \frac{2\sqrt{2}}{\pi}\frac{V_{out}}{j\omega M_1}\cdot\sin\left(\frac{\gamma_1}{2}\right) = \frac{2\sqrt{2}}{\pi}\frac{V_{out}}{j\omega M_2}\cdot\sin\left(\frac{\gamma_2}{2}\right), \tag{R2}$$

where γ_1 and γ_2 are the conducting angles of the active rectifiers. As shown in Fig. R9, the output sides of the rectifiers are paralleled to each other. Thus, only when $\dfrac{\sin\left(\gamma_1/2\right)}{M_1} = \dfrac{\sin\left(\gamma_2/2\right)}{M_2}$ is achieved, the formula (R2) can be set up. However, with the possible misalignment conditions of the magnetic coupler, formula

(R2) can be hard to set up while the conducting angles γ_1 and γ_2 are regulated for efficiency improvement. Then, the circulation phenomenon will easily occur with a sharp decrease in the system output power and the overall efficiency. Therefore, the SS compensated WPT systems always utilize the diode rectifier with the DC-DC converter for rectification and power regulation.

2) For the LCC-LCC compensation networks

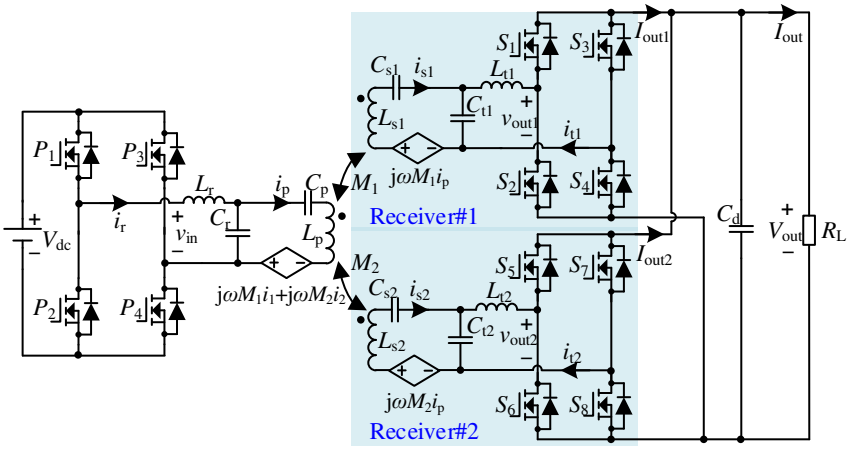

Fig. R10. The dual-receiver WPT system with LCC-LCC compensation network.

When the LCC-LCC compensated WPT system is resonant, the currents in the LCC-LCC compensated WPT can be obtained as

$$\begin{cases} \dot{I}_{\mathrm{r}} = \dot{V}_{\mathrm{in}(1)} \cdot \left(\dfrac{M_1^2 Z_{\mathrm{eq1}}}{\omega^2 L_{\mathrm{r}}^2 L_{\mathrm{t1}}^2} + \dfrac{M_2^2 Z_{\mathrm{eq2}}}{\omega^2 L_{\mathrm{r}}^2 L_{\mathrm{t2}}^2} \right) & \dot{I}_{\mathrm{p}} = \dfrac{\dot{V}_{\mathrm{in}(1)}}{j\omega L_{\mathrm{r}}} \\ \dot{I}_{\mathrm{s1}} = \dot{V}_{\mathrm{in}(1)} \cdot \dfrac{M_1 Z_{\mathrm{eq1}}}{\omega^2 L_{\mathrm{r}} L_{\mathrm{t1}}^2} & \dot{I}_{\mathrm{t1}} = -\dot{V}_{\mathrm{in}(1)} \cdot \dfrac{M_1}{j\omega L_{\mathrm{r}} L_{\mathrm{t1}}} \\ \dot{I}_{\mathrm{s2}} = \dot{V}_{\mathrm{in}(1)} \cdot \dfrac{M_2 Z_{\mathrm{eq2}}}{\omega^2 L_{\mathrm{r}} L_{\mathrm{t2}}^2} & \dot{I}_{\mathrm{t2}} = -\dot{V}_{\mathrm{in}(1)} \cdot \dfrac{M_2}{j\omega L_{\mathrm{r}} L_{\mathrm{t2}}} \end{cases} . \tag{4}$$

According to (4), it is evident that the transmitter coil current I_{p} is independent of the mutual inductance and the equivalent impedance of the rectifiers. Thus, the unbalance of the mutual inductance, and the equivalent impedance will not result in the circulation phenomenon in the LCC-LCC compensated WPT system with the active rectifiers.

The MATLAB/Simulink models of the dual-receiver WPT system with SS compensation and LCC compensation are set up, respectively, and results are shown in Fig. R11. In the SS compensated WPT system, while the mutual inductances are balanced, the currents in the two receiver coils are also balanced, as shown in Fig. R11(a). However, the circulation occurs when mutual inductances of receivers are different, as shown in Fig. R11(b). The current i_{t1} in the receiver coil with a smaller mutual inductance will lead the voltage v_{out1} to input the rectifier, and the amplitude of i_{t1} is reduced for balancing voltages output of the two rectifiers. Additionally, the amplitude of the receiver #2 coil current i_{t2} with a larger

mutual inductance is significantly increased, and the phase remains. Therefore, the characteristic of the constant current in the SS compensated WPT system is affected. The reactive power in receiver#1 not only occupies the limited power transfer capacity of the channel, but also produces huge extra power loss.

In the LCC-LCC compensated WPT system, there is no circulation in the system when mutual inductances of receivers are different, as shown in Fig. R11(c) and (d). No matter how much the difference between the two mutual inductances is, the constant current characteristic of the LCC-LCC compensation networks is still maintained, and the current ratio is always equal to the mutual inductance ratio.

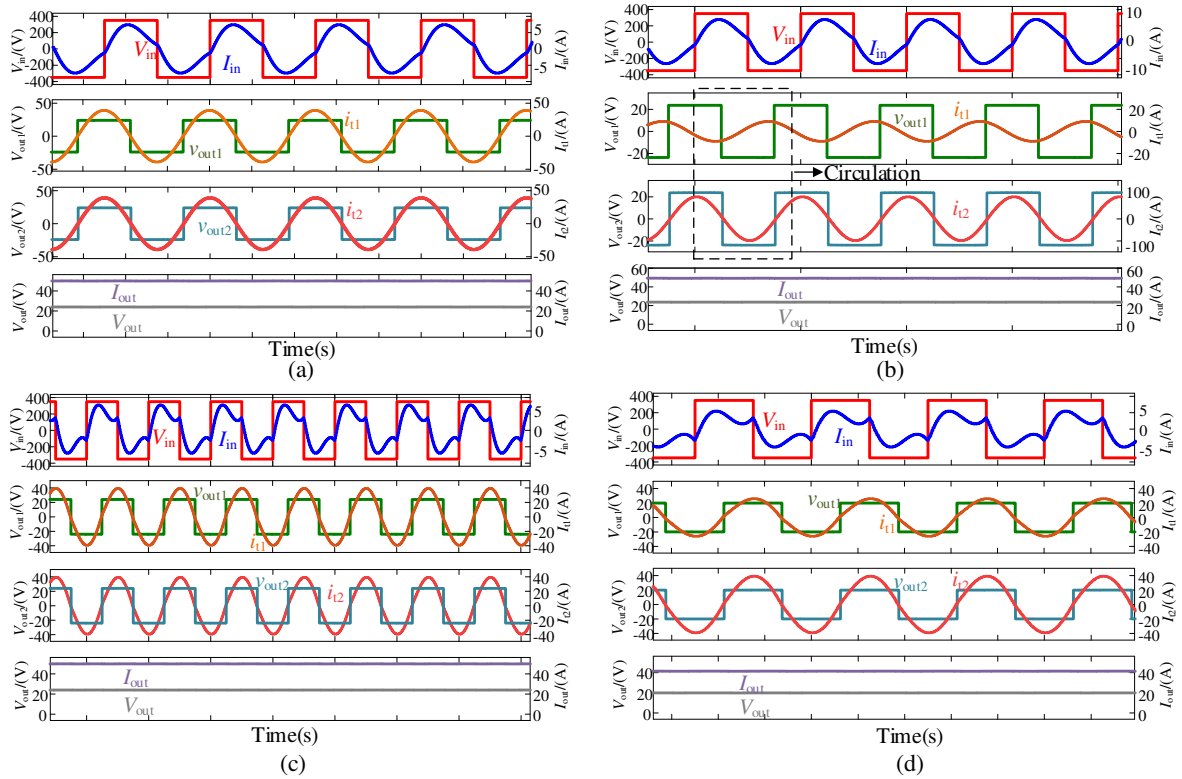

Fig. R11. The key waveforms of the SS compensated system (a) with M_1=M_2; (b) M_1=0.66M_2, and the LCC-LCC compensated system (c) with M_1=M_2; (d) M_1=0.66M_2

(2) The transmitter side circuit in Fig. 3 is not marked with Ir, so it is suggested to modify Fig. 3

Response: Thanks for your careful review. We have corrected this issue in the revised manuscript, and the modifications are highlighted in **red**.

(3) The second formula of formula (2) is the voltage equation of the transmitting circuit. Your derivation does not include the voltage of capacitor Cp and the voltage of Lp. The capacitance Cp and the capacitance Cr are not equal. How do you derive this formula?

Response: Thanks for your careful review. We are sorry that we provided an incomplete equation and confused you. However, the derivation of the final loop currents is correct.

Here, the complete equation (2) should be

$$\begin{cases} \dot{V}_{\text{in}(1)} = \left(j\omega L_{\text{r}} + \frac{1}{j\omega C_{\text{r}}}\right)\dot{I}_{\text{r}} - \frac{1}{j\omega C_{\text{r}}}\cdot\dot{I}_{\text{p}} \\ 0 = j\omega M_1\dot{I}_{\text{s1}} + j\omega M_2\dot{I}_{\text{s2}} + \frac{1}{j\omega C_{\text{r}}}\cdot\dot{I}_{\text{r}} + \left(j\omega L_{\text{p}} + \frac{1}{j\omega C_{\text{r}}} + \frac{1}{j\omega C_{\text{p}}}\right)\dot{I}_{\text{p}} \\ 0 = j\omega M_1\dot{I}_{\text{p}} + \left(j\omega L_{\text{s1}} + \frac{1}{j\omega C_{\text{s1}}} + \frac{1}{j\omega C_{\text{t1}}}\right)\dot{I}_{\text{s1}} - \frac{1}{j\omega C_{\text{t1}}}\cdot\dot{I}_{\text{t1}} \\ 0 = j\omega M_2\dot{I}_{\text{p}} + \left(j\omega L_{\text{s2}} + \frac{1}{j\omega C_{\text{s2}}} + \frac{1}{j\omega C_{\text{t2}}}\right)\dot{I}_{\text{s2}} - \frac{1}{j\omega C_{\text{t2}}}\cdot\dot{I}_{\text{t2}} \\ \dot{V}_{\text{out1}(1)} = \left(j\omega L_{\text{t1}} + \frac{1}{j\omega C_{\text{t1}}}\right)\dot{I}_{\text{t1}} - \frac{1}{j\omega C_{\text{t1}}}\cdot\dot{I}_{\text{s1}} \\ \dot{V}_{\text{out2}(1)} = \left(j\omega L_{\text{t2}} + \frac{1}{j\omega C_{\text{t2}}}\right)\dot{I}_{\text{t2}} - \frac{1}{j\omega C_{\text{t2}}}\cdot\dot{I}_{\text{s2}} \end{cases}, \tag{2}$$

where

$$\begin{cases} C_{\text{r}} = (\omega^2 L_{\text{r}})^{-1} & C_{\text{p}} = \left(\omega^2\left(L_{\text{p}} - L_{\text{r}}\right)\right)^{-1} \\ C_{\text{t1}} = (\omega^2 L_{\text{t1}})^{-1} & C_{\text{s1}} = \left(\omega^2\left(L_{\text{s1}} - L_{\text{t1}}\right)\right)^{-1} \\ C_{\text{t2}} = (\omega^2 L_{\text{t2}})^{-1} & C_{\text{s2}} = \left(\omega^2\left(L_{\text{s2}} - L_{\text{t2}}\right)\right)^{-1} \end{cases}. \tag{1}$$

Here, since the transmitter coil L_{p}, the compensated capacitor C_{p} and C_{r} are serial resonant, their impedances can be compensated completely, which means that

$$\left(j\omega L_{\text{p}} + \frac{1}{j\omega C_{\text{r}}} + \frac{1}{j\omega C_{\text{p}}}\right)\dot{I}_{\text{p}} = 0\,. \tag{R3}$$

Thus, the initial formula and its derivation results are correct.

To avoid misleading reviewers and other readers again, we have revised equation (R2) into (R1) in the revised manuscript, and the modifications are highlighted in **red**.

(4) What are the reasons for the errors of M1 and M2 in the simulation and experiment in Fig. 13? Is the error within a reasonable range?

Response: Thanks for your valuable comments. **The errors of M_1 and M_2 in the simulation and experiment are mainly caused by the difference between the handmade magnetic coupler and the ideal MAXWELL model.** Frankly, these errors are contingent and difficult to eliminate completely.

Although we can accurately control the air gap between the transmitter coil and the receiver coils, some other geometric parameters like the area of the coils, the distances between the coils and the ferrites and the stacked angle of the two BP coils may not be adjusted very accurately. These issues may slightly affect the mutual inductances between the transmitter coil and receiver coils. Meanwhile, the simulation model in MAXWELL is solved by finite element analysis, and there may be some errors between the simulation results and the actual situation, especially when the distance between the transmitter coil and

the receiver coils are large. However, in Fig. 13, the simulated and measured mutual inductance trends against the misalignment distance are very consistent. We believe the error is acceptable and can be used to guide the design of system parameters.

In the revised manuscript, a new magnetic coupler is designed to suit the 50A output current. The MAXWELL software is also adopted for assisting coupler design. The simulation model and the dimensions are shown in Fig. R12. The simulated and measured mutual inductances between the transmitter coil and the receiver coil against the misalignment distance are plotted in Fig. R13. Here, due to the reasons mentioned above, the errors between M_1 and M_2 in the simulation and experiment still exist. However, **these errors are still limited and acceptable.**

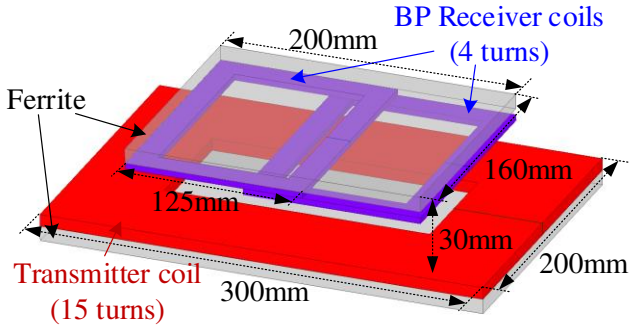

Fig. R12. The model and dimensions of the magnetic couplers.

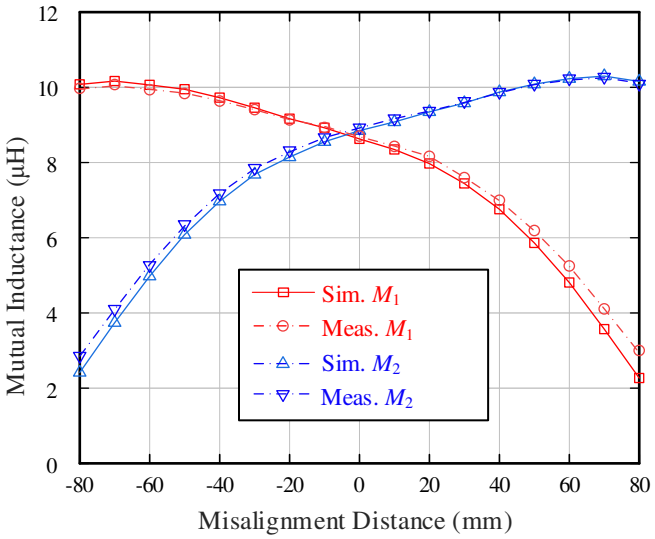

Fig. R13. The mutual inductance between the transmitter coil and the single receiver coil against the misalignment distance.

(5) Are the two coils in the manuscript designed to be the same size? What is the reason for this design? If one of the coils is designed to be smaller, so that the power can pass through the small coils as much as possible, the coil loss can be effectively reduced in low voltage and high current occasions.

Response: Thanks for your valuable comments. Indeed, in some designs of DC-DC converters with the PPP control [R10]-[R13], the power channels are always divided into the main channel and the auxiliary power channel. The majority of power is transferred through the main channel with a large transformer

winding, and the auxiliary channel processes the minor power with a small transformer winding for power regulation. Thus, a lower overall power loss can be achieved since less power is processed.

However, this paper adopts the BP coil structure on the receiver side to improve the misalignment tolerance of the WPT system. For the Light Electric Vehicles (LEVs) wireless charging applications, we cannot anticipate the vehicles' misalignment direction and distance. Here, the two receiver coils are designed almost identical. Thus, no matter the LEV is parked on the left or right, at least one of the receiver coils can be used as the main power channel, and the other one can be regarded as the auxiliary power channel, as shown in Fig. R14. Then, the system output power can be guaranteed with different misalignment conditions.

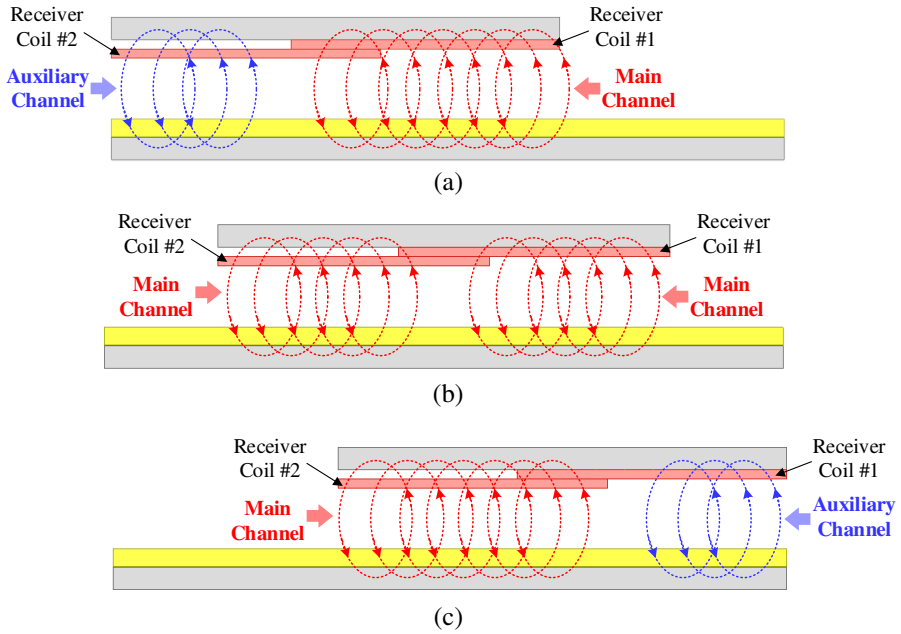

Fig. R14. Schematic diagram of power transfer with two channels under different misalignment conditions (a)on the left, (b) well-aligned, (c) on the right.

[R10]D. Neumayr, M. Vöhringer, N. Chrysogelos, G. Deboy, and J. Kolar, "P3DCT—partial-power pre-regulated DC transformer," in *IEEE Trans. on Power Electron.*, vol. 34, no. 7, pp. 6036-6047, Jul. 2019.

[R11]J. Zientarski, M. Martins, J. Pinheiro, and H. Hey, "Evaluation of power processing in series-connected partial-power converters," in *IEEE J.Emerg. Sel. Topics Power Electron.*, vol. 7, no. 1, pp. 343-352, March. 2019.

[R12]V. Iyer, S. Gulur, G. Gohil, and S. Bhattacharya, "An approach towards extreme fast charging station power delivery for electric vehicles with partial power processing," in *IEEE Trans. on Ind. Electron.*, vol. 67, no. 10, pp. 8076-8087, Oct. 2020.

[R13]J. Anzola, I. Aizpuru, A. Arruti, A. Alacano, and C. Bernal, "Review of architectures based on partial power processing for DC-DC applications," in *IEEE Access*, vol. 8, pp. 103405-103418, Jun. 2020.

(6) In this paper, ZVS operations of the inverter and rectifier are achieved, please the author provides the waveforms of the Vds and Vgs of the MOSFET to certify the achievement of the ZVS operation. According to (10), a fuzzy range of β1 (β2) for the ZVS condition is given, please explain how to design

the specific parameter of β1 (β2) in the close-loop control.

Response: Thanks for your valuable comments. **For the design of the phase difference angle between the input current and the voltage of the active rectifier β_1 and β_2, the parasitic parameters of the driver and the converter should be well considered.** The following will analyze the design of this parameter from both theoretical and experimental perspectives.

The basic model of the MOSFET is shown in Fig. R15(a), and the equivalent model of the MOSFET is shown in Fig. R15(b). Here, some parasitic elements are illustrated. C_{gs}, C_{gd} and C_{ds} are the interelectrode capacitance of the MOSFET; $C_{oss}=C_{ds}+C_{gd}$ is defined as the output capacitor of MOSFETs. R_{mg}, R_{md} and R_{ms} are the parasitic resistors, which are series-connected to the gate, the drain, and the MOSFET source. While analyzing the switching process of the MOSFETs, these parasitic capacitors are essential.

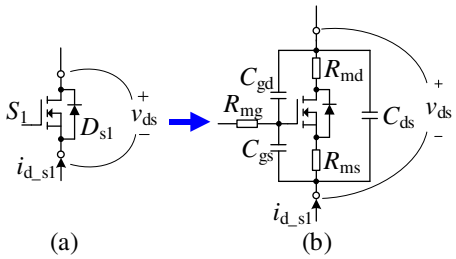

Fig. R15. (a) MOSFET schematic, (b) the MOSFET equivalent circuit.

The schematic diagram of the active rectifier in the WPT system is illustrated in Fig. R16(a), and the typical key waveforms for the ZVS operation of the rectifier in the proposed WPT system is illustrated in Fig. R16(b). Here, the process for S_2 turning off and S_1 turn on is analyzed as an example. **The key to achieve ZVS operation is that the drive signal of S_1 should be pulled to high after the drain-source voltage v_{ds_s1} is decreased to 0.** Thus, there will be no crossover of the waveforms of the current flowing through the MOSFET and the drain-source voltage, which means there is no turn-on loss on the MOSFET. Here, to analyze the prerequisites for the ZVS operation, the dead time σ_d of the rectifier drive signal should be carefully considered and designed.

As shown in Fig. R16(b), after the drive signal of S_2 is turned to the low level, it takes a period t_f before the gate-source voltage v_{gs_s2} drops to a certain level and S_2 is completely turned off. After S_2 is completely turned off, it takes another period time t_{oss} to reduce v_{ds1} to 0, the drive signal of S_1 can be turned to a high level. Thus, the dead time σ_d should cover these two periods of time. The calculation processes of t_f and t_{oss} are introduced as follow.

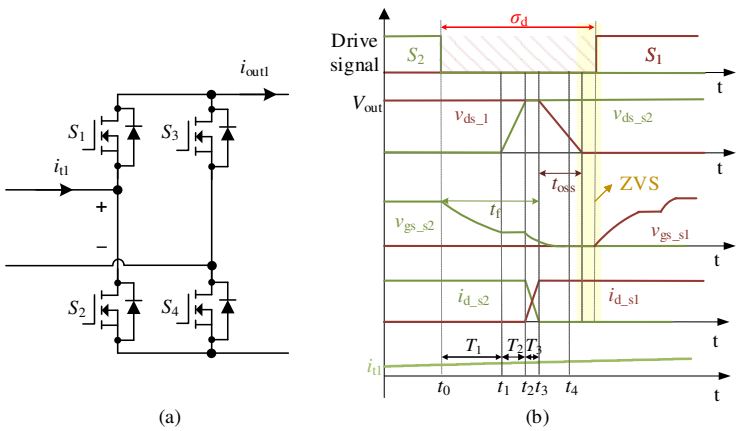

Fig. R16. (a) The schematic diagram of the active rectifier in the WPT system, (b) typical key waveforms for the ZVS operation of the rectifier in the proposed WPT system.

1) The turn off process of the MOSFETs

As shown in Fig. R16(b), from the drive signal of S_2 turn to low level until S_2 is completely turned off, there is another period t_f, and this period can be divided into these three stages:

Stage1 [t_0-t_1]: In this stage, the gate-source capacitor C_{gs_s2} is discharged through the gate resistance and the driver circuit, the gate-source voltage v_{gs_s2} decreases exponentially, and the duration can be calculated as

$$T_1 = T_g \cdot \ln\left(\frac{V_{driver} - V_{sat}}{V_t + I_0 / g - V_{sat}}\right), \tag{R4}$$

where V_{driver} is the gate-driven voltage; V_t is the gate threshold voltage; T_g is the RC time constant of the gate; I_o is equal to the drain current I_d here; g is the transconductance; V_{sat} is the driving circuit pull-down transistor saturation voltage drop, which can be obtained in the data sheet of the manufacturer or be determined by the design of the driver circuit.

Stage2 [t_1-t_2]: The gate voltage is in the plateau period, the reverse transfer capacitor C_{gd_s2} starts to be charged by i_{d_s2}, and the drain-source voltage v_{ds_s2} increases until it reaches V_{out}. Thus, the duration T_2 can be expressed as

$$T_2 = \frac{V_{out} \cdot C_{gd} \cdot R_{drive}}{V_t + I_0 / g - V_{sat}}, \tag{R5}$$

where R_{drive} is the gate series-connected resistance, including the internal and external resistance.

Stage3 [t_2-t_3]: In this stage, v_{gs_s2} continues to decline to V_t exponentially, and the drain current i_{d_s2} decreases to zero. The duration T_3 can be can be given as

$$T_3 = T_g \cdot \ln\left(\frac{V_t + I_0 / g - V_{sat}}{V_t - V_{sat}}\right). \tag{R6}$$

After t_3, S_2 is completely turned on, then t_f can be calculated as

$$t_{\mathrm{f}} = T_1 + T_2 + T_3 . \tag{R7}$$

2) The discharging process of C_{oss}

For achieving the ZVS operation, completely discharging the stored charge in the equivalent output capacitance C_{oss} of S_1 before the drive signal of S_1 is turned to a high level is necessary. Here, to simplify the analysis while ensuring the ZVS operation of the MOSFETs, we can consider that the equivalent output capacitance C_{oss} starts to discharge by i_{d_s1} at time t_3. Thus, the discharging time t_{oss} can be calculated as follow.

While S_2 is conducting, the drain-source voltage v_{ds_s1} is equal to V_{out}, and the charge stored on the equivalent output capacitance C_{oss} can be expressed as

$$Q_{s1} = C_{oss} V_{out} . \tag{R8}$$

To discharge C_{oss} in the switching process, when the drive signal of S_2 turns to a low level, the rectifier input current i_{t1} must be reverse to positive, or the ZVS operation cannot be achieved. The relationship between toss and Q_{s1} can be expressed as

$$Q_{s1} = \int_0^{t_{oss}} \frac{\sqrt{2}}{2} I_{t1} \sin\left(\omega t + \varphi_1\right) \cdot \mathrm{d}t , \tag{R9}$$

where I_{t1} is the RMS value of the input current of the active rectifier, and φ_1 is the phase difference between the positive-to-negative zero-crossing point of i_{t1} and S_1.

Substituting (R9) into (R8), t_{oss} can be solved as

$$t_{oss} = \frac{\left| \arccos\left[\cos\left(\varphi_1\right) - \frac{\sqrt{2}\omega C_{oss} V_{out}}{I_{t1}} \right] - \varphi_1 \right|}{\omega} . \tag{R10}$$

According to (R10), we can draw this conclusion that the larger φ_1 is, the discharging current of C_{oss} is higher, which could shorter the discharging process. Thus, while φ_1=0, the maximum discharging time t_{oss_max} can be calculated as

$$t_{oss\_max} = \frac{\left| \arccos\left[1 - \frac{\sqrt{2}\omega C_{oss} V_{out}}{I_{t1}} \right] \right|}{\omega} . \tag{R11}$$

Moreover, to guarantee C_{oss} is discharged completely, the toss always be set larger than t_{oss_max} in the experiment.

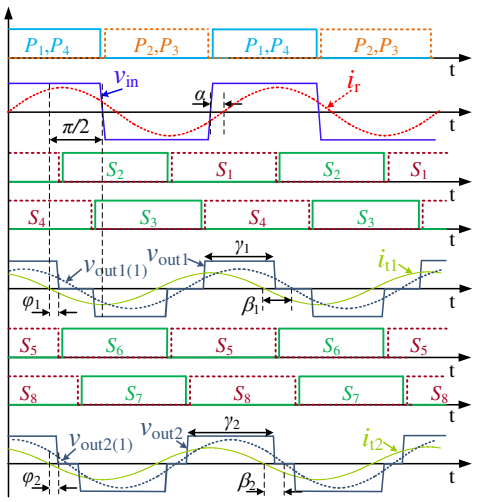

Fig. R17. Waveforms of VAPS control based dual-receiver WPT system.

In conclusion, to cover these two periods t_f and t_{oss}, the dead time should satisfy $\sigma_d \geq t_{oss\_max}+t_f$. However, to ensure the ZVS operation and limit the dead time not to be too large, φ_1 and φ_2 are always reserved as a tiny positive value. Thus, the waveforms of the VAPS control based dual-receiver WPT system are shown in Fig. R17. To ensure the ZVS operation of the rectifiers, β_1 and β_2 must satisfy

$$\begin{cases} \beta_1 = \varphi_1 + \dfrac{\pi - \gamma_1}{2} \\ \beta_2 = \varphi_2 + \dfrac{\pi - \gamma_2}{2} \end{cases}. \tag{R12}$$

In the revised manuscript, a 24V-50A low-voltage-high-current output WPT system is designed with adopting IXFX420N10T as the MOSFETs in the rectifiers. According to the parameters in TABLE RV, **we can get a set of parameters of dead time σ_d=300ns and the phase difference φ_1=φ_2=5°. Then, the ZVS operation can be achieved in the active rectifiers.** It should be noted that in the above analysis process, to ensure the realization of ZVS operation under different high-frequency conditions, σ_d, φ_1 and φ_2 time has already retained a large margin, and it is no longer necessary to amplify them.

TABLE RV

PARAMETER VALUES FOR THE MOSFET AND THE RECTIFIER CIRCUIT

Symb.	*Val.*	*Symb.*	*Val.*
V_{drive}	15V	V_t	2.5V
C_{oss}	4.65nF@24V	C_{gd}	550pF@24V
V_{sat}	0.2V (Typical)	T_g	118ns
R_{drive}	2.46Ω (Including the internal and external)	I_0/g	0.2 (Approximate value)

The experimental results of the ZVS operation of the MOSFET S_1 in the rectifier are shown in Fig. R18. While the rectifier is regulated by the VAPS modulation method and conducting angle γ_1 is set as 0°, 50° and 110°, the ZVS operation can be achieved in all conditions.

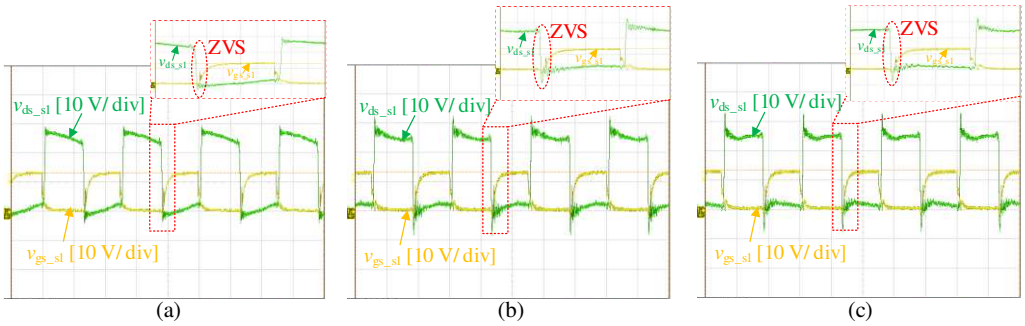

Fig. R18. Experimental waveforms of v_{ds_s1} and v_{gs_s1} while the conducting angle γ_1 is set as (a) 0°, (b) 50° and (c) 110°.

Moreover, with the MOSFETs C3M0021120D adopted in the inverter, a similar method for designing the dead time for achieving the ZVS operation can also be used. However, these kinds of MOSFETs are more accessible to achieve the ZVS operation due to the advantages of the SiC MOSFETs. The experimental result of the ZVS operation of the MOSFET P_1 in the inverter is shown in Fig. R19. While the conducting angles of the rectifier γ_1 and γ_2 are set as 0°, which indicates the passive power and the turn-off current of the MOSFETs are small, the ZVS operation is still achieved in this condition.

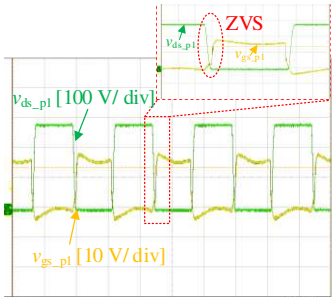

Fig. R19. Experimental waveforms of v_{ds_p1} and v_{gs_p1} while the conducting angles of the rectifiers γ_1 and γ_2 are set as 0°.

■ **Reviewer: #3**

Comments to the Author:

(1) The main claimed contribution from this manuscript is that a Partial Power Processing (PPP) control can be used to adjust each receiver operating at full or nearly no load in which the switching off loss is negligible thus the efficiency can be improved. The PPP is based on reallocating the load flow via two receivers. However, I am confused by one fundamental issue of the entire idea. If it is a dual-receiver WPT, should two receivers for two independent loads? The dual-receiver WPT is commonly considered for light EV charging where multiple or two light EVs such as two e-scooters can be wirelessly charged by one transmitter (station). The confusing part is that the authors have depicted a dual-receiver WPT connected in parallel to one single load in this manuscript, as shown in Fig 1. Is it still a dual-receiver WPT? The authors should realize that, if it is a proper dual-receiver WPT, the loads are independent to each other and the entire work of this manuscript, by reallocating power flow between two receivers, becomes groundless.

Response: Thanks for your review. We are very sorry that our inaccurate description confused you about the "dual receiver". In this paper, **the dual receiver WPT system is designed to increase the power transfer capacity and improve the overall system efficiency,** and similar ideas are already reported in many literatures [R14], [R15].

Here, **each receiver consists of the same receiver coil, compensation network and the active rectifier. The output of the active rectifiers is connected in parallel.** Thus, the system output current is the sum of the output current of each active rectifier, and the output current of each receiver is independent to the other. Then, since the output currents of the receivers are inputted to the same load, a power regulation method or a power flow reallocating method for improving the overall system efficiency in each power channel is necessary.

[R14]A. Zaheer, G. Covic, and D. Kacprzak, "A bipolar pad in a 10-kHz 300-W distributed IPT system for AGV applications," in *IEEE Trans. Ind. Electron.*, vol. 61, no. 7, pp. 3288–3301, Jul. 2014.

[R15]Y. Li, T. Lin, R. Mai, L. Huang and Z. He, "Compact Double-Sided Decoupled Coils-Based WPT Systems for High-Power Applications: Analysis, Design, and Experimental Verification," in *IEEE Trans. Transp. Electrif.*, vol. 4, no. 1, pp. 64-75, March 2018.

(2) If the 'dual-receiver' WPT in this manuscript is deemed to have one signal load, then it is more appropriate to compare with single receiver system. The work from this manuscript might be meaningful, subject to thorough investigation and substantial revision work in a completely different system and comparison.

Response: Thanks for your valuable review and suggestion. We have rebuilt a 24V-50A output WPT system in the revised manuscript. Meanwhile, **according to your suggestion, a single receiver system is also built to provide a fair and complete comparison.**

The circuit topologies of the dual receivers WPT system and single receiver WPT system are shown in Fig. R20. Meanwhile, the model and dimensions of the magnetic couplers are shown in Fig. R21. Compared to the dual receiver system, the current stress of the receiver coil and the active rectifier are doubled in the single receiver system. Moreover, while regulating the system output current, the large 50A output current will be processed with a single active rectifier, which caused a vast switching loss.

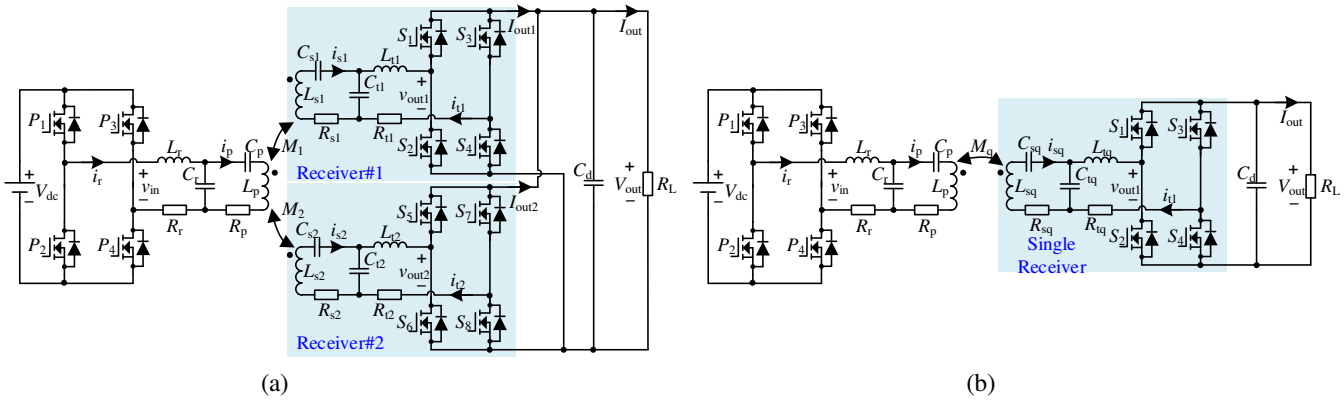

Fig. R20. Schematic diagram of (a) the dual-receiver WPT system and (b) the single receiver with LCC-LCC compensation network.

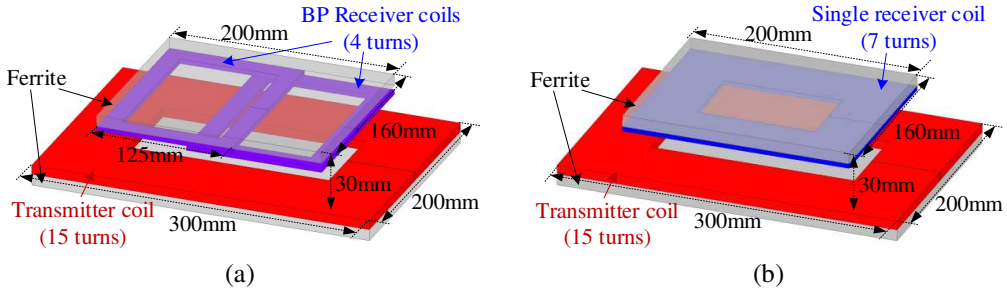

Fig. R21. The model and dimensions of the magnetic couplers (a) with the BP receiver coils and (b) the single Q receiver coil.

The key parameters of the dual receiver and single receiver systems are listed in TABLE RVI and TABLE VII. The coils of the magnetic coupler in the rebuilt experimental setup are shown in Fig. R22.

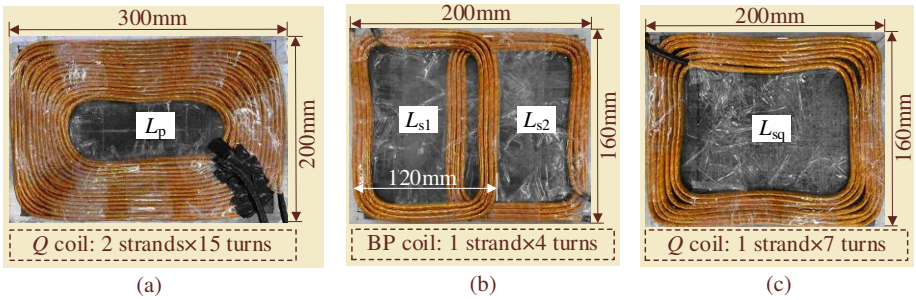

Fig. R22. Structure and dimensions of (a) the transmitter coil, (b) the BP receiver coils and (c) the single large receiver coil.

By regulating the active rectifier with the Variable Angle Phase Shift (VAPS) modulation method, the system output power can be regulated, and the trends of power transfer efficiency against the output power are also plotted in Fig. R23. **Apparently, the efficiency of the dual-receiver WPT system is much**

higher than that of the single receiver WPT system with the whole operation range under different misalignment conditions. Meanwhile, with the 24V-50A output WPT system, the proposed PPP control method still performs well in improving the overall system efficiency by reallocating the load flow via two receivers, which is the main contribution of this manuscript.

TABLE RVI

SYSTEM SPECIFICATION AND PARAMETER VALUES OF THE DUAL RECEIVER WPT SYSTEM

Symb.	*Val.*	*Symb.*	*Val.*	*Symb.*	*Val.*
V_{dc}	350V	V_{out}	24V	I_{out}	5~50A
L_r	29.5uH	C_r	21.46nF	R_r	40mΩ
L_p	90.4uH	C_p	10.4nF	R_p	220.1mΩ
L_{t1}	2.63uH	C_{t1}	240.8nF	R_{t1}	2.9mΩ
L_{t2}	2.64uH	C_{t2}	239.9nF	R_{t2}	2.9mΩ
L_{s1}	6.92uH	C_{s1}	147.6nF	R_{s1}	23.0mΩ
L_{s2}	7.09uH	C_{s2}	142.3nF	R_{s2}	24.1mΩ
f	200kHz	S_1-S_8	IXFX420N10T	A_{rec}+ B_{rec}	138ns
Air gap	30mm	P_1-P_4	C3M0021120D	A_{inv}+ B_{inv}	34.2ns

TABLE VII

SYSTEM SPECIFICATION AND PARAMETER VALUES OF THE SINGLE RECEIVER WPT SYSTEM

Symb.	*Val.*	*Symb.*	*Val.*	*Symb.*	*Val.*
V_{dc}	350V	V_{out}	24V	I_{out}	5~50A
L_r	29.5uH	C_r	21.46nF	R_r	40mΩ
L_p	90.4uH	C_p	10.4nF	R_p	220.1mΩ
L_{tq}	14.4uH	C_{tq}	53.8nF	R_{tq}	60.1mΩ
L_{sq}	2.64uH	C_{sq}	239.9nF	R_{sq}	2.5mΩ
f	200kHz	S_1-S_8	IXFX420N10T	A_{rec}+ B_{rec}	138ns
Air gap	30mm	P_1-P_4	C3M0021120D	A_{inv}+ B_{inv}	34.2ns

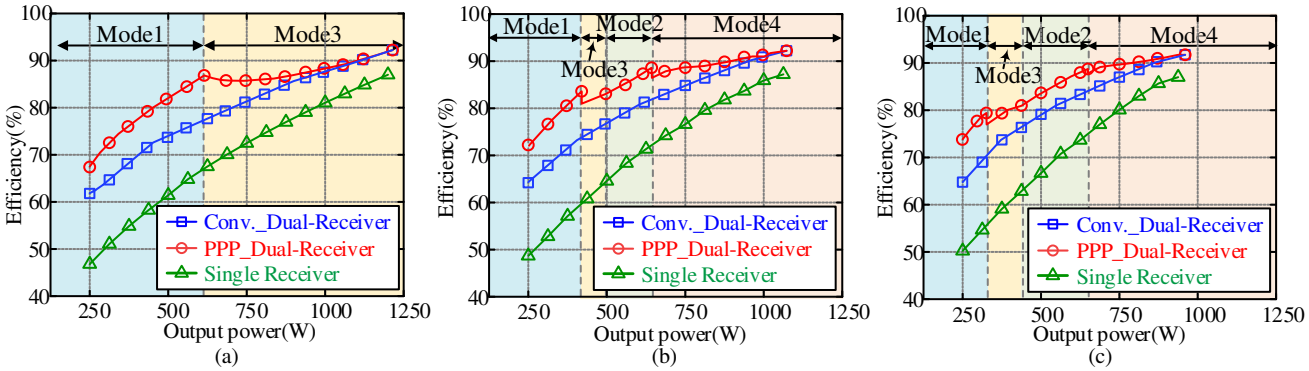

Fig. R23. The efficiency trend of the dual receiver system and the single receiver system with (a) M_1=M_2, (b) M_1=0.66M_2, and (c) M_1=0.5M_2.

(3) The other technical issue is loss calculation. I am not sure the Eoff values used by the authors and the information is missing. The authors claim that the Eoff in (26) is from the device datasheet but the device IXFK170N20T has not given Eoff at the datasheet. In fact, most of low voltage MOSFETs do not give Eoff in their datasheets and this value is subject to testing/modelling by users. It is also incorrect to

have Eoff as a fixed value in (26), Eoff varies therefore the result of loss analysis might be invalid.

Response: Thanks for your careful review. We are very sorry that we missed the value of E_{off} in the last edition of the manuscript. Meanwhile, we must apologize for the slip that "E_{off}, U_{DD}, I_D, Q_{DD}, and I_{R_D} are some inherent parameters of the MOSFETs, which can be found or fitted in the datasheet.". As the reviewer mentioned, these values of this kind should be tested or modelled by users. With the modelling method introduced in [R16], [R17], the turn-off energy of the high-frequency MOSFETs, even the low voltage Si MOSFETs, can be well calculated. Additionally, the turn-off energy is not a fixed value exactly. However, this parameter is also nearly proportional to the turn-off current of the MOSFET and the DC output voltage of the rectifier. **Thus, an available but straightforward method to evaluate the turn-off energy of the MOSFETs with different switching currents and output voltages is to calculate or test a specific value of E_{off_test} with its test turn-off current I_D and voltage U_{DD}.** Then, when the switching condition is changed, the approximate value of the turn-off energy can be calculated as

$$E_{off} = \frac{E_{off\_test}}{U_{DD} \cdot I_D} \cdot I_{sw} \cdot V_{sw}, \tag{R13}$$

where I_{sw} and V_{sw} are the corresponding actual current and voltage at the switching point.

In the proposed WPT system, while evaluating the turn-off loss of the active rectifiers, I_{sw} can be regarded as the real-time value of the rectifier input sinusoidal current when the MOSFET is turned off, and V_{sw} can be regarded as the output voltage of the rectifier V_{out}. Thus, the turn-off energy of the single active rectifier in the proposed WPT system with the variable angle phase shift modulation method can be expressed as

$$\begin{cases} E_{turn\_off1} = \dfrac{E_{off\_test}}{U_{DD} \cdot I_D} \cdot \left(2\sqrt{2} I_{t1} \left(\left|\sin\left(\varphi_1\right)\right| + \left|\sin\left(\varphi_1 + \pi - \gamma_1\right)\right|\right)\right) V_{out} \\ E_{turn\_off2} = \dfrac{E_{off\_test}}{U_{DD} \cdot I_D} \cdot \left(2\sqrt{2} I_{t2} \left(\left|\sin\left(\varphi_2\right)\right| + \left|\sin\left(\varphi_2 + \pi - \gamma_2\right)\right|\right)\right) V_{out} \end{cases}, \tag{R14}$$

where E_{turn_off1} and E_{turn_off2} are the turn-off energy of the active rectifier in Receiver#1 and Receiver#2, respectively. **Although the calculation results of the turn-off energy may not be wholly accurate, and it is possible to be influenced by the high order harmonics and parasitic parameters of the main power circuit and the driver circuit, the results still have a substantial reference value.**

With the rebuilt experimental setup in the revised manuscript, a 24V-50A low-voltage-high-current system is built and analyzed. The ultra-low conducting resistance MOSFETs IXFX420N10T are selected as the switch devices of the active rectifiers. Based on the mathematical model in [R17], the datasheet of IXFX420N10T and the other parameters of the rectifier, the turn-off energy is calculated as about 130uJ (@ U_{DD}=24V and I_D=40A). The experimental and calculated results of the rectifier power loss under

different misalignment conditions are shown in Fig. R24. Although there are some unavoidable errors between the calculated and experimental results, they are still consistent overall, proving the reliability of this calculation model of the turn-off energy.

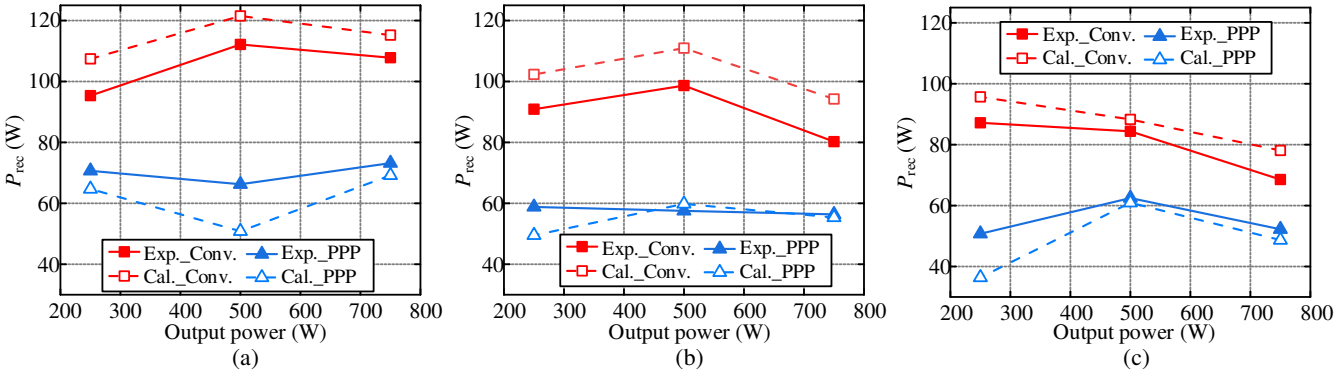

Fig. R24. The experimental and calculated power loss of rectifiers with (a) M_1=M_2, (b) M_1=0.66M_2, and (c) M_1=0.5M_2.

Based on these calculation results and the calculation model in (R14), the PPP control method and power distribution strategy are designed. The experimental results show the excellent performance of the proposed PPP control method in reducing the switching loss of the rectifiers and improving the system's overall efficiency.

[R16]D. Christen and J. Biela, "Analytical switching loss modelling based on datasheet parameters for MOSFETs in a half-bridge," in *IEEE Trans. on Power Electron.*, vol. 34, no. 4, pp. 3700-3710, Apr. 2019.

[R17] W. Eberle, Z. Zhang, Y. Liu and P. Sen, "A practical switching loss model for buck voltage regulators," in *IEEE Trans. on Power Electron.*, vol. 24, no. 3, pp. 700-713, Mar. 2009.

(4) The manuscript appears to have a smooth and coherent narrative. However, it lacks justification and rigour, and some technical analysis is likely to be incorrect or incomplete. Without substantial revision, it cannot be accepted.

Response: Thanks for your review. More technical details, analysis, and experimental comparisons are provided in the response file and the revised manuscript. Some detailed analysis and experimental setup are substantially revised, considering your and other reviewers' valuable and valuable comments and suggestions. We have made many changes in response to these comments and suggestions, and we hope our modification will satisfy you and the other reviewers.

■ **Reviewer: #4**

Comments to the Author

(1) It seems that only secondary loss is considered. Does there exist difference on the reflected impedance from the secondary to the primary with the proposed and conventional control schemes? If yes, how does the proposed control scheme affect the primary loss? From the waveforms and the analysis in Fig. 20, the inverter loss is also reduced, but what is the reason behind? Please explain.

Response: Thanks for your careful review. Indeed, there does exist difference on the reflected impedance from the secondary to the primary side with the proposed PPP control scheme and the conventional schemes, which even makes less inverter loss and the ESRs loss in the primary side in the WPT system with the proposed control schemes. The detailed analysis is introduced as follow.

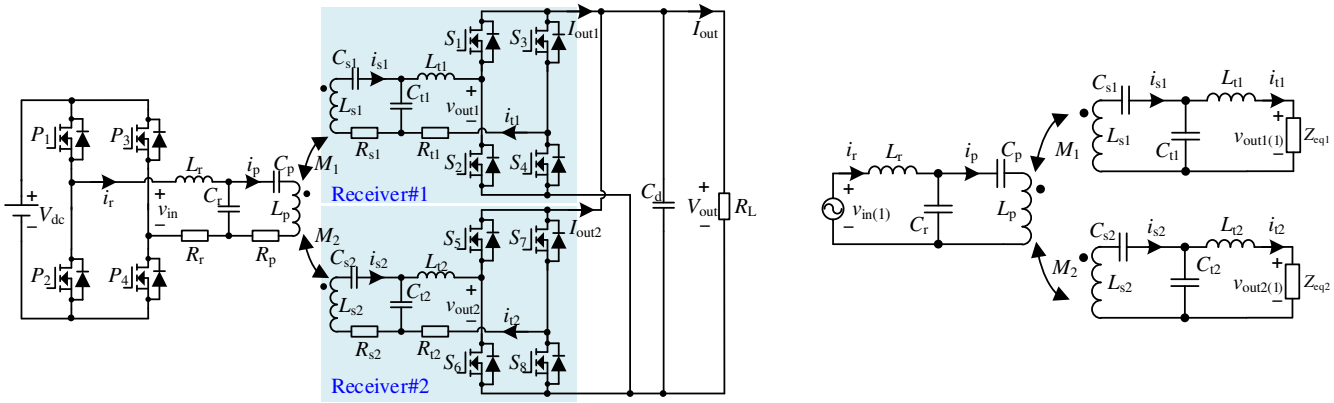

Fig. R25. (a) Schematic diagram and (b) the equivalent circuit of the proposed dual-receiver WPT system.

1) Reflected impedance analysis

The schematic diagram of the proposed dual-receiver WPT system is depicted in Fig. R25(a). At the same time, ignoring the ESRs of the passive elements and the power loss in the converters, the simplified AC equivalent circuit of the proposed WPT system can be depicted in Fig. R25 (b).

The Kirchhoff's voltage law can be listed as

$$\begin{cases} \dot{V}_{\text{in}(1)} = \left(j\omega L_{\text{r}} + \frac{1}{j\omega C_{\text{r}}}\right)\dot{I}_{\text{r}} - \frac{1}{j\omega C_{\text{r}}}\cdot\dot{I}_{\text{p}} \\ 0 = j\omega M_1\dot{I}_{\text{s1}} + j\omega M_2\dot{I}_{\text{s2}} + \frac{1}{j\omega C_{\text{r}}}\cdot\dot{I}_{\text{r}} + \left(j\omega L_{\text{p}} + \frac{1}{j\omega C_{\text{r}}} + \frac{1}{j\omega C_{\text{p}}}\right)\dot{I}_{\text{p}} \\ 0 = j\omega M_1\dot{I}_{\text{p}} + \left(j\omega L_{\text{s1}} + \frac{1}{j\omega C_{\text{s1}}} + \frac{1}{j\omega C_{\text{t1}}}\right)\dot{I}_{\text{s1}} - \frac{1}{j\omega C_{\text{t1}}}\cdot\dot{I}_{\text{t1}} \\ 0 = j\omega M_2\dot{I}_{\text{p}} + \left(j\omega L_{\text{s2}} + \frac{1}{j\omega C_{\text{s2}}} + \frac{1}{j\omega C_{\text{t2}}}\right)\dot{I}_{\text{s2}} - \frac{1}{j\omega C_{\text{t2}}}\cdot\dot{I}_{\text{t2}} \\ \dot{V}_{\text{out1}(1)} = \left(j\omega L_{\text{t1}} + \frac{1}{j\omega C_{\text{t1}}}\right)\dot{I}_{\text{t1}} - \frac{1}{j\omega C_{\text{t1}}}\cdot\dot{I}_{\text{s1}} \\ \dot{V}_{\text{out2}(1)} = \left(j\omega L_{\text{t2}} + \frac{1}{j\omega C_{\text{t2}}}\right)\dot{I}_{\text{t2}} - \frac{1}{j\omega C_{\text{t2}}}\cdot\dot{I}_{\text{s2}} \end{cases}, \quad (2)$$

where

$$\begin{cases} \dot{V}_{\text{out1(1)}} = \dot{I}_{\text{t1}} \cdot Z_{\text{eq1}} \\ \dot{V}_{\text{out2(1)}} = \dot{I}_{\text{t2}} \cdot Z_{\text{eq2}} \end{cases}. \tag{3}$$

Z_{eq1} and Z_{eq2} are the equivalent load impedances of the two active rectifiers at the receiver side. To ensure the resonance of each current loop, the compensation network should satisfy

$$\begin{cases} C_{\text{r}} = (\omega^2 L_{\text{r}})^{-1} & C_{\text{p}} = \left(\omega^2 \left(L_{\text{p}} - L_{\text{r}}\right)\right)^{-1} \\ C_{\text{t1}} = (\omega^2 L_{\text{t1}})^{-1} & C_{\text{s1}} = \left(\omega^2 \left(L_{\text{s1}} - L_{\text{t1}}\right)\right)^{-1} \\ C_{\text{t2}} = (\omega^2 L_{\text{t2}})^{-1} & C_{\text{s2}} = \left(\omega^2 \left(L_{\text{s2}} - L_{\text{t2}}\right)\right)^{-1} \end{cases}, \tag{1}$$

where $\omega=2\pi f$ is the operating angular frequency.

Then, to analyze the reflected impedance from the secondary to the primary side, the system equivalent circuit can be further depicted in Fig. R26. Z_f is the equivalent reflected impedance at the output side of the inverter, which is affected by the equivalent load impedances Z_{eq1} and Z_{eq2}.

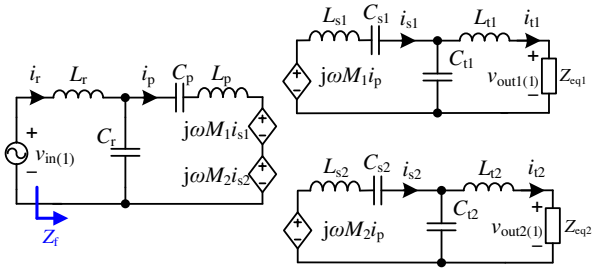

Fig. R26. The equivalent reflected impedance circuit of the proposed dual-receiver WPT system.

According to (1)-(2), the equivalent impedance Z_f reflected the primary side from the two receivers can be derived as

$$Z_{\text{f}} = \frac{\dot{V}_{\text{in(1)}}}{\dot{I}_{\text{r}}} = \frac{\omega^2 L_{\text{r}}^2}{\left(\frac{M_1^2}{L_{\text{t1}}^2} Z_{\text{eq1}} + \frac{M_2^2}{L_{\text{t2}}^2} Z_{\text{eq2}}\right)}. \tag{9}$$

In the proposed scheme, the variable angle phase shift (VAPS) modulation method regulates the active rectifiers, and the key waveforms are shown in Fig. R27. With the variable angle phase shift (VAPS) modulation method, Z_{eq1} and Z_{eq2} can be derived as

$$Z_{\text{eq1}} = \frac{\dot{V}_{\text{out1(1)}}}{\dot{I}_{\text{t1}}} = \frac{\omega L_{\text{r}} L_{\text{t1}} V_{\text{out}}}{V_{\text{dc}} M_1} \cdot \sin\left(\frac{\gamma_1}{2}\right) \cdot \left(\cos(\beta_1) + j \cdot \sin(\beta_1)\right), \tag{15}$$

and

$$Z_{\text{eq2}} = \frac{\dot{V}_{\text{out2(1)}}}{\dot{I}_{\text{t2}}} = \frac{\omega L_{\text{r}} L_{\text{t2}} V_{\text{out}}}{V_{\text{dc}} M_2} \cdot \sin\left(\frac{\gamma_2}{2}\right) \cdot \left(\cos(\beta_2) + j \cdot \sin(\beta_2)\right). \tag{R15}$$

where β_1/β_2 is the phase difference between the input current and voltage of the rectifier, and γ_1/γ_2 is the

conducting angle of the active rectifier. To ensure the ZVS operation of all the MOSFETs in these two rectifiers, γ_1/γ_2 and β_1/β_2 should satisfy

$$\begin{cases} \beta_1 = \varphi_1 + \dfrac{\pi-\gamma_1}{2} > \dfrac{\pi-\gamma_1}{2} \\ \beta_2 = \varphi_2 + \dfrac{\pi-\gamma_2}{2} > \dfrac{\pi-\gamma_2}{2} \end{cases}, \tag{11}$$

where φ_1/φ_2 is the phase difference between the positive-to-negative zero-crossing point of i_{t1}/i_{t2} and S_1/S_5, which should always be set as a positive value to ensure the ZVS operation in the rectifiers.

Thus, substituting (R15) and (15) into (9), the equivalent impedance Z_f can be obtained as

$$Z_f = \frac{\dot{V}_{in(1)}}{\dot{I}_r} = \frac{\omega L_r V_{dc}}{\left(\dfrac{M_1}{L_{t1}}\cdot\sin\left(\dfrac{\gamma_1}{2}\right)\cdot\left(\cos(\beta_1)+j\cdot\sin(\beta_1)\right)+\dfrac{M_2}{L_{t2}}\cdot\sin\left(\dfrac{\gamma_2}{2}\right)\cdot\left(\cos(\beta_2)+j\cdot\sin(\beta_2)\right)\right)\cdot V_{out}}. \tag{19}$$

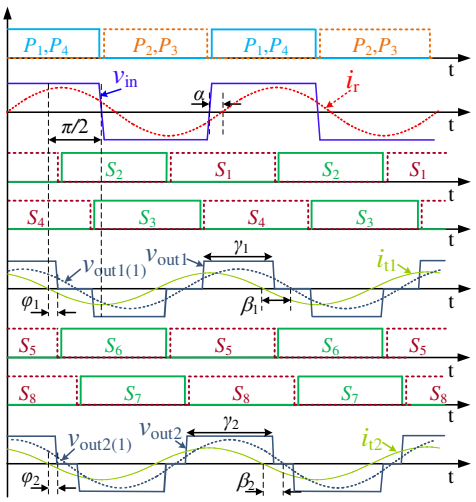

Fig. R27. Waveforms of VAPS control of the dual-receiver WPT system.

In the WPT system with the conventional power distribution method, the active rectifiers are controlled by the VAPS method to obtain the optimal current ratio to average the power losses between the two receivers. Therefore, the reflected impedance Z_{f_conv} of the receivers can be calculated as

$$Z_{f\_conv} = \frac{\omega L_r V_{dc}}{\left(\dfrac{M_1}{L_{t1}}+\dfrac{M_2}{L_{t2}}\right)\cdot\sin\left(\dfrac{\gamma}{2}\right)\cdot\left(\cos(\beta)+j\cdot\sin(\beta)\right)\cdot V_{out}}, \tag{R16}$$

where $\beta=\beta_1=\beta_2$ and $\gamma=\gamma_1=\gamma_2$, which indicate that the conducting angle and the phase difference between the input current and the voltage of both active rectifiers are the same.

In the WPT system with the proposed PPP control method, there is always only one active rectifier operating with the VAPS control method, and the other rectifier is shutting or full-load. According to the load power requirements, the operation modes for the two rectifiers can be divided into the following four modes, as shown in TABLE VIII. The specific methods and steps of mode division will not be repeated here, introduced in the revised manuscript in detail. Then, the reflected impedance Z_{f_PPP} can be obtained

as

$$Z_{\mathrm{f\_ppp}}=\begin{cases}\dfrac{\omega L_{\mathrm{r}}V_{\mathrm{dc}}}{\left(\dfrac{M_{\mathrm{i}}}{L_{\mathrm{ti}}}\cdot\sin\left(\dfrac{\gamma_{\mathrm{i}}}{2}\right)\cdot\left(\cos\left(\beta_{\mathrm{i}}\right)+j\cdot\sin\left(\beta_{\mathrm{i}}\right)\right)\right)\cdot V_{\mathrm{out}}}, & (\mathrm{i}=1,2) \quad Mode1,2. \\ \dfrac{\omega L_{\mathrm{r}}V_{\mathrm{dc}}}{\left(\dfrac{M_1}{L_{\mathrm{t1}}}\cdot\left(\cos\left(\beta_1\right)+j\cdot\sin\left(\beta_1\right)\right)+\dfrac{M_2}{L_{\mathrm{t2}}}\cdot\sin\left(\dfrac{\gamma_2}{2}\right)\cdot\left(\cos\left(\beta_2\right)+j\cdot\sin\left(\beta_2\right)\right)\right)\cdot V_{\mathrm{out}}}, & Mode3 \\ \dfrac{\omega L_{\mathrm{r}}V_{\mathrm{dc}}}{\left(\dfrac{M_1}{L_{\mathrm{t1}}}\cdot\sin\left(\dfrac{\gamma_1}{2}\right)\cdot\left(\cos\left(\beta_1\right)+j\cdot\sin\left(\beta_1\right)\right)+\dfrac{M_2}{L_{\mathrm{t2}}}\cdot\left(\cos\left(\beta_2\right)+j\cdot\sin\left(\beta_2\right)\right)\right)\cdot V_{\mathrm{out}}}, & Mode4\end{cases} \tag{R17}$$

TABLE VIII

OPERATION MODES OF THE RECTIFIERS IN FOUR MODES

Operation mode	The status of Rec#1	The status of Rec#2
Mode 1	VAPS	Shutting
Mode 2	Shutting	VAPS
Mode 3	Full-load	VAPS
Mode 4	VAPS	Full-load

Meanwhile, α is determined as the phase difference between the output current and voltage of the inverter, which can be expressed as

$$\alpha=\arctan\left(\frac{\mathrm{Im}\left(Z_{\mathrm{f}}\right)}{\mathrm{Re}\left(Z_{\mathrm{f}}\right)}\right). \tag{27}$$

The value of α indicates the proportion of the passive power in the WPT system. According to (R16), (R17), and (27), we can plot the trends of α against the system output current with two different power distribution methods. As shown in Fig. R28(a). Since keeping the other at full-load or shut-down conditions can minimize the proportion of passive power, the system with the proposed PPP method always has a lower α compared with the conventional method.

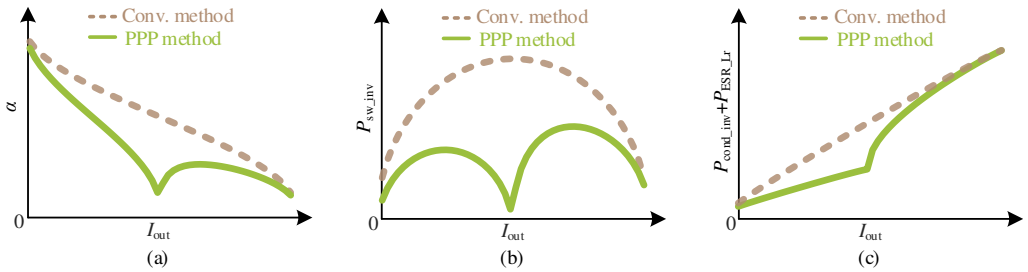

Fig. R28. Trends of (a) α, (b) $P_{\mathrm{sw\_inv}}$, and (c) $P_{\mathrm{ond\_inv}}+P_{\mathrm{ESR\_Lr}}$ against the system output current with two different power distribution methods while M_1=M_2.

2) Primary loss analysis

Moreover, with the imaginary part of Z_{f} decreasing, the switching loss and the conducting loss of the inverter and the ESRs loss in the primary side can also be reduced.

(a) The switching loss of the inverter

The inverter operates at a constant operating frequency *f*, a fixed duty cycle, and the zero phase-shift

angle. Thus, the ZVS operation can be easily achieved. Thus, the switching loss of the inverter can be expressed as

$$P_{sw\_inv} = 4\sqrt{2}\left(A_{inv} + B_{inv}\right)V_{in} I_r \sin(\alpha) f\,, \tag{26}$$

where A_{inv}=E_{off_inv}/($U_{DD\_inv}I_{D\_INV}$) dedicates the value of the turn-off energy of the MOSFETs in the inverter at the standard test condition, B_{inv}=Q_{DD_inv}/I_{RD_inv} dedicates the value of the switching loss of the anti-paralleled diodes. α is the phase difference between the output current and the output voltage of the inverter, as shown in Fig. R27. E_{off_inv}, U_{DD_inv}, I_{D_inv}, Q_{DD_inv}, and I_{RD_inv} are some inherent parameters of the MOSFETs, which can be fitted in the datasheet or tested/modelled by the users.

Therefore, we can find that the switching loss of the inverter is affected by the inverter output current I_r and the phase difference α. Here, combining (2), (R15) and (15), I_r can be solved as

$$I_r = V_{in(1)} \cdot \left(\frac{M_1^2 \left|Z_{eq1}\right|}{\omega^2 L_r^2 L_{t1}^2} + \frac{M_2^2 \left|Z_{eq2}\right|}{\omega^2 L_r^2 L_{t2}^2} \right) = \frac{2\sqrt{2}V_{out}}{\pi\omega L_r} \cdot \left(\frac{M_1}{L_{t1}} \cdot \sin\left(\frac{\gamma_1}{2}\right) + \frac{M_2}{\omega L_{t2}} \cdot \sin\left(\frac{\gamma_2}{2}\right) \right). \tag{R18}$$

Then, substituting (R18) and (27) into (26), the trends of the switching loss of the inverter can be plotted in Fig. R28(b). Obviously, **with lower reactive components of the reflected impedance Z_f and the inverter output current I_r, the switching loss of the inverter with the proposed PPP control method could be apparently reduced.**

(b) The conducting loss of the inverter and the primary ESRs loss

Ignoring the conducting loss on the anti-paralleled diodes of the MOSFETs, which occupies a tiny part of the overall power loss, the conducting loss of the inverter P_{cond} can be expressed as

$$P_{cond\_inv} = 2 \cdot I_r^2 \cdot R_{ds\_inv}\,, \tag{25}$$

where R_{ds_inv} dedicates the turn-on resistance of the MOSFET in the inverter. Meanwhile, although the current in the transmitter coil I_p is not affected by the load condition apparently, the ESR loss on the resonant inductor L_r can also be reduced with the decreasing of I_r. The ESR loss on this inductor can be defined as

$$P_{ESR\_Lr} = I_r^2 \cdot R_r\,. \tag{R19}$$

Thus, according to (R18), (25), and (R19), the trends of the sum of the inverter conducting loss and the ESR loss on L_r can be plotted in Fig. R28(c). With the reduced RMS value of I_r, the conducting loss and the ESR loss on L_r are decreased by adopting the PPP control method with the same system output current.

The experimental results of the primary loss are shown in Fig. R29. Compared with the conventional

control method, the proposed PPP control can effectively reduce the power loss of the inverter conducting and the ESR loss, which is consistent with the theoretical analysis.

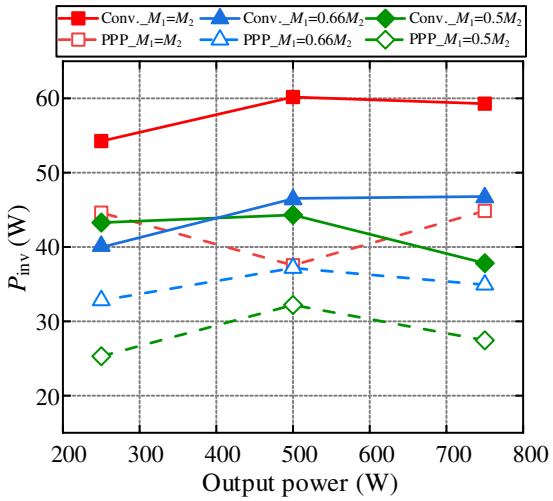

Fig. R29. The power loss of the transmitter side under different misalignment conditions.

(2) As shown in Fig. 7, there are multiple modes, how to ensure the seamless transition between these modes in the control diagram? Discussion on this issue is suggested.

Response: Thanks for your valuable review and suggestion. **In the experimental setup, both PI control and hysteresis control are adopted in the control system. PI control is used to ensure the stability of the output voltage in a single operation mode, while the hysteresis control is used to ensure the seamless transition between different operation modes.**

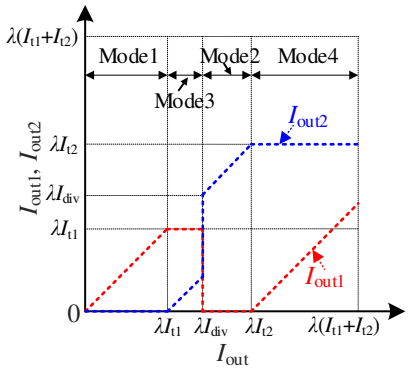

Fig. R30. The output current I_{out1} and I_{out2} against the load required current I_{out} with the proposed PPP control method.

As shown in Fig. R30, with the proposed PPP control method, the boundary lines between different operating modes include $\lambda I_{t1}, \lambda I_{t2}$ and λI_{div}, where $\lambda = \frac{2\sqrt{2}}{\pi}\cos(\varphi)$ and φ is a tiny positive angle. I_{div} can be obtained by sampling the value of I_{t1}, I_{t2} and calculating based on the power loss model. Based on this operation modes division strategy, a valuable and straightforward hysteresis control method can be designed.

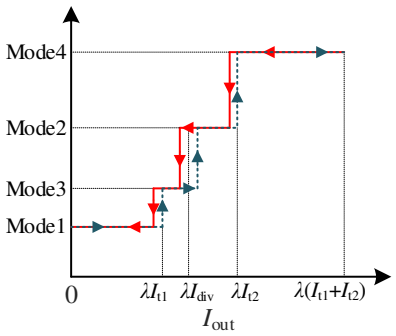

Fig. R31. The diagram of the designed hysteresis control with the proposed PPP control method.

The diagram of the designed hysteresis control is shown in Fig. R31. To avoid the frequent switching between the different operation modes, the hysteresis curve and switching points are designed considering the characteristics of Mode 1~Mode 4. The details of the proposed hysteresis control are introduced as follow.

1) Switch between Mode 1 and Mode 3

Due to the limitation of the output current in Mode 1, while the required system output current I_{out} increased to λI_{t1}, Receiver#1 cannot provide more power. Thus, the operation mode should be switched to Mode 3 at $I_{out}=\lambda I_{t1}$. However, while the receiver operates in Mode 3, the extra power loss is produced by regulating the active rectifier in Receiver#2, which decreases the minimal system output power of Mode 3. Thus, based on some experimental tests, when the receiver operation mode switches from Mode 3 to Mode 1, the hysteresis switching point can be set at $I_{out}=0.98\cdot\lambda I_{t1}$.

2) Switch between Mode 3 and Mode 2

There is a large amount of overlap in the power coverage of Mode 3 and Mode 2, so it is actually easier to design a hysteresis control curve between the two modes. With the experimental test results, while the required I_{out} increases and the operation mode switches from Mode 3 to Mode 2, the switching point can be set at $I_{out}=1.02\lambda I_{div}$. On the other hand, the other switching point for I_{out} decreasing can be designed at $I_{out}=0.98\lambda I_{div}$.

3) Switch between Mode 2 and Mode 4

Similarly, due to the limitation of the output current in Mode 2, while the required system output current I_{out} increased to λI_{t2}, Receiver#2 cannot provide more power individually, and the operation mode should be switched to Mode 4 at $I_{out}=\lambda I_{t2}$. Moreover, there is also a tiny part of overlap in the power coverage of mode 2 and mode 4 caused by regulating the active rectifier in Receiver#1. Therefore, when the receiver operation mode switches from Mode 4 to Mode 2, the hysteresis switching point can be set at $I_{out}=0.98\cdot\lambda I_{t2}$.

To verify the actual effect of the designed hysteresis control and the corresponding PI control, the

dynamic response waveforms of receiver mode switching are also provided in Fig. R32. Whether the operating mode is switching or not, the output voltage V_{out} can be maintained at a constant value without apparent oscillation or fluctuation. The waveforms of i_{s1} and i_{s2} show that the control system with the proposed hysteresis control works very well, and no frequent switching is observed, which indicates the seamless transition and well dynamic performance of the control system.

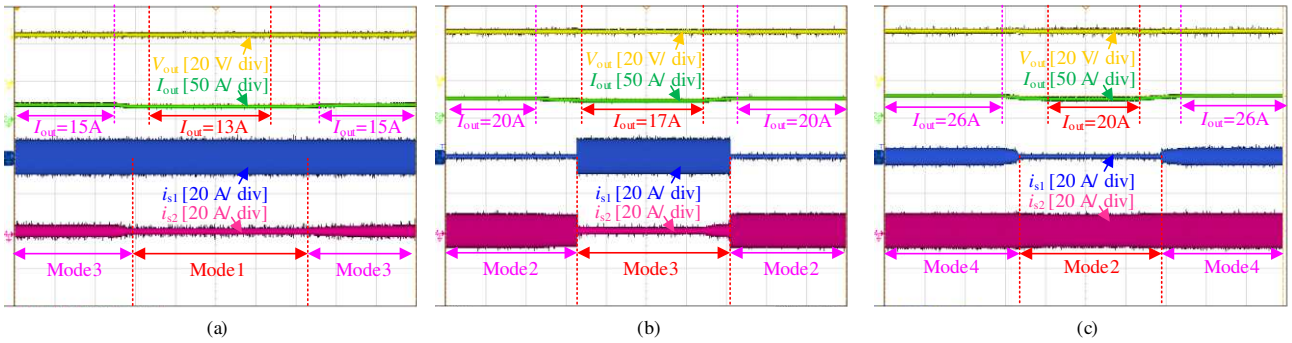

Fig. R32. Experimental dynamic response waveforms of V_{out}, I_{out}, i_{s1}, i_{s2} while (a) switching between Mode 1 and Mode 3, (b) switching between Mode 3 and Mode 2, and (c) switching between Mode 2 and Mode 4.

(3) The control diagram shown in Fig. 7 seems to be useful in static applications with misalignment problems. Can it apply on dynamic applications? How to ensure fast dynamic response?

Response: Thanks for your valuable review. We have supplemented the experiment about the dynamic WPT system with a low speed, as shown in Fig. R33.

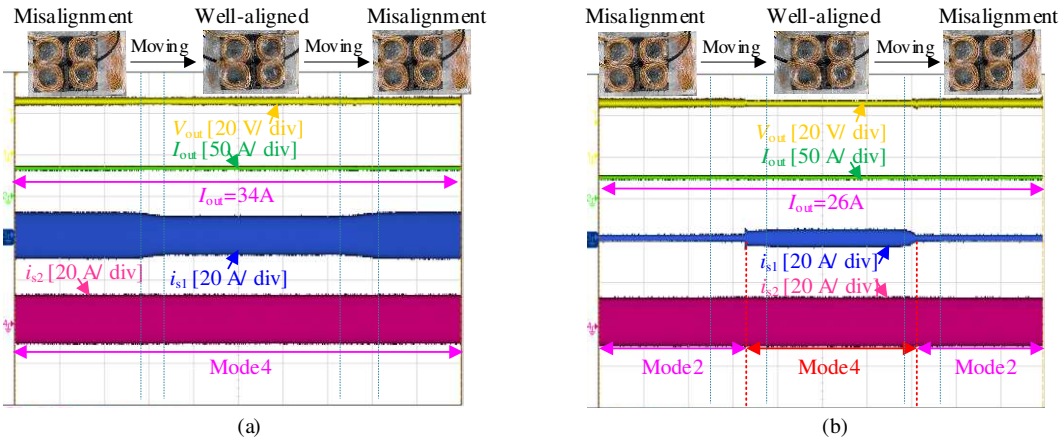

Fig. R33. Experimental dynamic response waveforms of V_{out}, I_{out}, i_{s1}, i_{s2} while (a) I_{out}=34A and (b) I_{out}=26A.

When the output current keeps constant as 34A, the output voltage of the system can be maintained at the required value while the receiver is moving, and the receiver operates in Mode 4 stably, as shown in Fig. R33(a). When the output current is varied to 26A, the designed hysteresis control will regulate the system operate in the corresponding operating mode with different misalignment conditions, as shown in Fig. R33(b). Meanwhile, the output voltage can be maintained with the PI control without any obvious overshoot or oscillation. Moreover, **benefits from the designed hysteresis control strategy and**

corresponding PI control, the output of the system performs excellent dynamic response and stability in the low-speed dynamic conditions.

(4) Compared with the conventional control, is any additional effort paid to implement the proposed control?

Response: Thanks for your review. In the produced control method, compared to the conventional control, the additional hardware may be the current sensors in the receiver side, which are utilized to sample the RMS values of the active rectifiers' input currents and provide the basis of receiver operation mode selection. Moreover, due to the demands of operation mode switching, a hysteresis control strategy is adopted in the control system. Cause there is no DC/DC converters or other large-sized devices for power regulating, the additional effort paid to implement the proposed control is well limited.

Finally, we appreciate the reviewer and editor for thought provoking discussion and valuable comments. The paper has been carefully checked and revised again. We hope that this version is up to the standard of publication.